

**FEDERAL UNIVERSITY OF SANTA CATARINA
MECHANICAL ENGINEERING DEPARTMENT**

Lauro Augusto Jeronimo Oliveira

**THERMODYNAMIC MODELING OF A PARABOLIC TROUGH
CONCENTRATED SOLAR POWER PLANT WITH MOLTEN SALT AS HEAT
TRANSFER FLUID**

Florianópolis/SC - Brazil
2019

**FEDERAL UNIVERSITY OF SANTA CATARINA
MECHANICAL ENGINEERING DEPARTMENT**

Lauro Augusto Jeronimo Oliveira

**THERMODYNAMIC MODELING OF A PARABOLIC TROUGH
CONCENTRATED SOLAR POWER PLANT WITH MOLTEN SALT AS HEAT
TRANSFER FLUID**

Monograph presented to the Mechanical Engineering course at the Federal University of Santa Catarina as a partial requirement to obtain the Bachelor's Degree in Mechanical Engineering.

Advisor: Prof. Dr. Júlio Cesar Passos

Co-Advisor: Prof. Dr. Herbert Zondag -
Eindhoven University of Technology (NL)

Florianópolis/SC - Brazil
2019

Jeronimo Oliveira, Lauro Augusto
THERMODYNAMIC MODELING OF A PARABOLIC
TROUGH
CONCENTRATED SOLAR POWER PLANT WITH
MOLTEN SALT AS HEAT TRANSFER FLUID / Lauro
Augusto Jeronimo Oliveira ; orientador, Julio Cesar
Passos, coorientador, Herbert Zondag, 2019.
85 p.

Trabalho de Conclusão de Curso (graduação) -
Universidade Federal de Santa Catarina, Centro
Tecnológico, Graduação em Engenharia Mecânica,
Florianópolis, 2019.

Inclui referências.

1. Engenharia Mecânica. 2. Energia heliotérmica . 3.
Tecnologia de calhas parabólicas. 4. Sais fundidos. 5.
Modelagem termodinâmica. I. Passos, Julio Cesar. II.
Zondag, Herbert. III. Universidade Federal de Santa
Catarina. Graduação em Engenharia Mecânica. IV.
Título.

Lauro Augusto Jeronimo Oliveira

**THERMODYNAMIC MODELING OF A PARABOLIC TROUGH CONCENTRATED
SOLAR POWER PLANT WITH MOLTEN SALT AS HEAT TRANSFER FLUID**

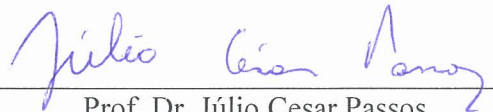
This Monograph has been evaluated as suitable as a requirement to the attainment of the Title of Mechanical Engineer, and its final version has been approved by the Examining Committee and the Mechanical Engineering Undergraduate Program of the Federal University of Santa Catarina.

Florianópolis- SC, 01 de fevereiro de 2019.



Prof. Dr. Carlos Enrique Niño Bohórquez
Undergraduate Program Coordinator

Examining Committee:



Prof. Dr. Júlio Cesar Passos
Advisor
Universidade Federal de Santa Catarina

Prof. Dr. Saulo Güths
Universidade Federal de Santa Catarina

Prof. Dr. Edson Bazzo
Universidade Federal de Santa Catarina

To my father, Robson (*in memoriam*).

Run, rabbit run
Dig that hole, forget the sun
And when at last the work is done
Don't sit down, it's time to dig another one
(Breath – Pink Floyd)

ACKNOWLEDGMENTS

Getting the present monograph done and finishing the Mechanical Engineering Bachelor took a long journey that started before I even got to the university. Throughout this journey, I have encountered many people that deserve my most sincere thanks for their role my life and in the achievement of this work.

To Professor Júlio Passos head of the Boiling Division of the Laboratory of Energy Conversion Processes Engineering and Technologies (LEPTEN), for his support and advisory in the development of this work.

To Professors Bart van Esch and the readiness to help with all, I needed to develop myself to my best during the exchange period in the Netherlands.

To Professor Herbert Zondag for advising me through the internship in the Eindhoven University of Technology (TU/e) in which a significant part of this work was done.

To my mother, Marcia Cruz for her guidance, support, and love that allowed me to see opportunities and explore the world. To my sister Linda Beatriz for her genuine love for me. To my step-father Edivan Cruz to whom I entrust two of my most precious treasures and whom I respect profoundly.

To my girlfriend Ananda Elisa for having patience and giving me love.

To Wanderley Peres and his mom, Dona Assuntina Lima, for their support and care on my arrival and stay in Florianópolis.

To the friends whom I met in Aracaju, Florianópolis, and Europe, in unique to the Brothers group, to the 'Bravos Companheiros,' to the TU/e's Erasmus friends, the Turma do Rolêa and friends in the Boiling Lab, for the fun moments, encouragement and support.

To Vitor Pigozzo and Alexandre Bittencourt for their advisory and help with the research.

To the Federal University of Santa Catarina (UFSC), the Department of Mechanical Engineering and its professors and staff for making attaining this degree possible.

To Coordination of Improvement of Higher Education Personnel of the Brazilian Government (Capes) that through its partnership with the Dutch organization for internationalization in education (NUFFIC) and the funding of the academic exchange program Capes/NUFFIC, that allowed my studies in the Netherlands from which part of this work originates.

To all others that somehow contributed in the making of this work.

RESUMO

Este trabalho trata do desenvolvimento do modelo de uma planta heliotérmica que utiliza a tecnologia de concentração de calhas parabólicas e sais fundidos como fluido de transferência de calor, assim como da avaliação do potencial de geração elétrica da referida planta para a localidade de Bom Jesus da Lapa (BA), semiárido do nordeste brasileiro. Os modelos físicos dos diferentes componentes e suas integrações assim como o modelo de operação da planta foram implementados nos softwares Matlab e Engineering Equation Solver (EES). Os modelos propostos foram simulados para uma planta de múltiplo solar igual a 2 e capacidade de armazenamento de 15h, durante um ano meteorológico típico, em intervalos de tempo de 1 hora. A partir dessa simulação, foram obtidos dados relativos à energia elétrica produzida, o fator de capacidade e a eficiência solar-elétrica da planta para o período de um ano assim como suas distribuições mensais. Os resultados indicam que a geração de energia elétrica da planta estão fortemente ligadas ao regime de chuvas, e por tanto de nebulosidade da região. A geração de eletricidade é maior nos meses secos, de abril a setembro, que nos meses úmidos, de outubro a março. Também, pode-se verificar que o modelo desenvolvido representa bem o sistema modelado.

Palavras-chave: Energia heliotérmica, Tecnologia de calhas parabólicas, Sais fundidos, Modelagem termodinâmica.

ABSTRACT

This work deals with the development of a model for a concentrated solar power plant with parabolic trough concentration technology and molten salts as heat transfer fluid as well as of the evaluation of the electric generation potential of said plant for Bom Jesus da Lapa (BA), a location at the semi-arid region of northeastern Brazil. The physical models of the different components and their integrations and the operation model of the plant were implemented in MATLAB and Engineering Equation Solver (EES) software. The proposed models were simulated for a plant with a solar multiple of 2 and with a storage capacity of 15h during a typical meteorological year at 1-hour time intervals. From this simulation data, the generated electric power on the plant and its capacity factor and solar-electric efficiency were determined on a monthly distribution and for a year. The results indicate that the electric power generation of the plant is strongly linked to the regime of rainfall, and cloudiness, of the region. Electricity generation is higher in the dry months, from April to September than in the humid months, from October to March. Also, it could be verified that the model developed in this work represents the modeled system well.

Keywords: Concentrated solar power plant, Parabolic trough technology, Molten salt, Thermodynamic modeling

LIST OF FIGURES

Figure 1 - Direct, diffuse and global irradiance.....	20
Figure 2 - Concentrated solar power plant conceptual scheme	21
Figure 3 - Concentration technologies classification chart	22
Figure 4 - Parabolic trough collector.....	23
Figure 5 - Schematics of a shortened heat collect element.....	25
Figure 6 - Main angles to characterize this sun-plane position relationship and the sun's position in the sky for a parabolic trough collector.....	27
Figure 7 - Collector mutual shading.....	29
Figure 8 - Heat collector element end loss	29
Figure 9 - Solar field loop	30
Figure 10 - Active storage arrangements: a - indirect two-tank, b – indirect thermocline, c – direct two-tank and d – direct thermocline	31
Figure 11 - Modeled plant schematics.....	34
Figure 12 - Direct Normal Irradiance (DNI) distribution in Brazil.....	35
Figure 13 - Plant information flow schematics	37
Figure 14 - Solar field information flow schematics.....	37
Figure 15 - Heat transfer phenomena and temperature distribution across the HCE.....	43
Figure 16 - SEGS VI power block layout	53
Figure 17 - Modeled Rankine cycle layout and thermodynamic cycle points	54
Figure 18 - Annual distribution of hourly DNI	58
Figure 19 - Annual distribution of cloudiness in BJJ	59
Figure 20 - Annual distribution of monthly cumulative solar field incoming radiant energy.....	59
Figure 21 - Annual distribution of monthly cumulative solar field thermal energy output	60
Figure 22 - Annual distribution of monthly average dry bulb ambient temperature.....	60
Figure 23 - Annual distribution of monthly average solar field thermal efficiency.....	61
Figure 24 - Annual distribution of monthly cumulative net electrical power output.....	62
Figure 25 - Annual distribution of monthly average solar-to-electric efficiency.....	62
Figure 26 - Annual distribution of the capacity factor	63

LIST OF TABLES

Table 1 - CSP technologies characteristics.....	23
Table 2 - Operation temperature and cost comparison between the heat transfer fluid Solar Salt, Hitec Salt, Hitec XL Salt, and the Therminol VP-1	26
Table 3 - Geographic coordinates of Bom Jesus da Lapa	36
Table 4 - Main characteristic parameters of Eurotrough ET-150 solar collector.....	38
Table 5 - Main characteristic parameters of the HCEMS-11 receiver	38
Table 6 - Solar field nominal parameters	48
Table 7 - Thermal energy storage nominal parameters	52
Table 8 - Rankine cycle thermodynamic parameters	55
Table 9 - Power block nominal parameters	55
Table 10 - Main plant electric generation parameters	61
Table 11 - Main Annual performance parameters.....	63
Table 12 - SAM's model parameters.....	64
Table 13 - Model results comparative table	65

LIST OF ABBREVIATIONS

BA	State of Bahia
BJL	Bom Jesus da Lapa
CSP	Concentrated Solar Power
CST	Concentrated Solar Thermal
DNI	Direct Normal Irradiance
DSG	Direct Steam Generation
EES	Engineering Equation Solver
ENEA	Italian National Agency for New Technologies, Energy and Sustainable
HCE	Heat Collector Element
HTF	Heat Transfer Fluid
LCOE	Levelized Cost of Energy
NREL	National Renewable Energy Laboratory
NSRDB	NREL National Radiation Database
PCM	Phase-change material
PE	Pernambuco
PTC	Parabolic Trough Collector
RN	Rio Grande do Norte
SAM	System Advisor Model
SCA	Solar Collector Assembly
SEGS	Solar Energy Generating Systems
TES	Thermal Energy Storage
TMY	Typical Meteorological Year
USD	United States Dollars

LIST OF SYMBOLS

Latin letters

A	Area	[m ²]
B	Solar time correction input parameter	[-]
c	Specific heat	[J/(kg·°C)]
D	Diameter	[m]
E	Solar time correction	[min]
E_{TES}	TES thermal capacity	[MWh]
f_f	Friction factor	[-]
g	Rankine cycle point	[-]
h	Enthalpy	[kJ/kg]
h'	Heat transfer coefficient	[W/(m ² ·°C)]
H	Height	[m]
L	Length	[m]
m	Mass	[kg/ton]
\dot{m}	Mass flow rate	[kg/s]
N	Number of	[-]
Nu	Nusselt number	[-]
NTU	Number of transfer units	[-]
P	Pressure	[bar]
Pr	Prandtl number	[-]
P_{gross}	Gross electrical power output	[GWh]
P_{net}	Net electrical power output	[GWh]
\dot{q}	Thermal energy rate	[W]
\dot{q}'	Thermal energy linear flux	[W/m]
Q	Thermal energy	[J]
R	Resistance	[Ω]
Ra	Rayleigh number	[-]
Re	Reynolds number	[-]
s	Entropy	[J/(kg·°C)]
$Shift$	Longitude shift	[deg]
SM	Solar multiple	[-]
$StopCrit$	Stop criteria	[-]
t	Time	[h]
T	Temperature	[°C]
\bar{T}	Average temperature	[°C]
U	Internal energy	[J]
UA	Overall heat transfer coefficient	[KW/°C]
\dot{W}	Turbine mechanical power output	[MW]
x	Steam quality	[-]
y	Day of the year	[-]

Greek letters

α	Absorptivity	[-]
β	Volumetric expansion coefficient	[-]
γ_{θ}	Intercept factor	[-]
δ	Declination	[-]
Δt	Time step length	[h]
ε	Effectiveness	[-]
ζ	Emittance	[-]
η	Efficiency	[-]
η_{clean}	Cleanliness factor	[-]
$\eta_{EndLoss}$	End loss factor	[-]
η_{IAM}	Incidence angle modifier	[-]
η_{opt}	Optical efficiency	[-]
$\eta_{opt,0^{\circ}}$	Peak optical efficiency	[-]
η_{Shadow}	Mutual shading factor	[-]
θ	Incidence angle	[deg]
θ_z	Solar zenith angle	[deg]
κ	Thermal Conductivity	[-]
λ	Longitude	[]
μ	Dynamic viscosity	[N.s/]
ρ	Density	[kg/m ³]
σ	Stefan-Boltzmann constant	[W/ (m ² K ⁴)]
τ	Transmissivity	[-]
φ	Latitude	[deg]
ψ	Reflector mirror reflectivity	[-]
ω	Hour angle	[deg]

Subscripts

<i>abs</i>	Absorber tube
<i>ABS</i>	Absorbed
<i>abs_abs</i>	Conduction through the absorber tube
<i>abs_env</i>	Radiation between the absorber tube and the glass envelope
<i>air</i>	Air
<i>amb</i>	Ambient
<i>ap</i>	Aperture
<i>av</i>	Available
<i>btw_rows</i>	Between collector rows
<i>btw_sca</i>	Between collector assemblies
<i>cond</i>	Condenser
<i>controller</i>	Mass flow rate controller
<i>CT</i>	Cold Tank

<i>e</i>	Electric
<i>eco</i>	Economizer
<i>eff</i>	Effective
<i>env</i>	Glass envelop
<i>env_amb</i>	Convection between the glass envelope and the environment
<i>env_env</i>	Conduction through the glass envelope
<i>env_sky</i>	Radiation between the glass envelope and the environment
<i>eva</i>	Evaporator
<i>f</i>	Focal
<i>FConv</i>	Forced convection
<i>FP</i>	Freezing protection
<i>gross</i>	Gross rate
<i>gross_to_net</i>	Gross to net conversion
<i>guess</i>	Guess value
<i>HL</i>	Heat loss
<i>HPturb</i>	High-pressure turbine
<i>HT</i>	Hot tank
<i>HTF</i>	Heat transfer fluid
<i>HTF_abs</i>	Convection between HTF and absorber tube
<i>i</i>	Inner or Inlet
<i>loc</i>	Local
<i>loop</i>	Loop
<i>LPturb</i>	Low-pressure turbine
<i>max</i>	Maximum
<i>min</i>	Minimum
<i>Nconv</i>	Natural convection
<i>net</i>	Net rate
<i>nom</i>	Nominal
<i>o</i>	Outer or Outlet
<i>past</i>	Past iteration
<i>PB</i>	Power block
<i>pump</i>	Pump
<i>ref</i>	Reference
<i>reh</i>	Reheater
<i>SCA</i>	Solar collector assembly
<i>SF</i>	Solar field
<i>sky</i>	Sky (as a black body)
<i>Sol</i>	Solar
<i>std</i>	Standard
<i>sup</i>	Superheater
<i>Tank</i>	Storage tank

<i>TES</i>	Thermal energy storage
<i>th</i>	Thermal
<i>USEFUL</i>	Useful
<i>var</i>	Mass flow rate controller stop criteria variation

TABLE OF CONTENTS

1	INTRODUCTION	16
1.1	OBJECTIVE	17
1.1.2	General objective	17
1.1.3	Specific objectives	17
1.2	STRUCTURE OF DOCUMENT	18
2	BACKGROUND	19
2.1	SOLAR ENERGY	19
2.2	CONCENTRATED SOLAR POWER SYSTEMS	20
2.2.1	Solar concentration technologies.....	21
2.3	PARABOLIC TROUGH COLLECTOR.....	23
2.3.1	Heat collector element	24
2.3.2	Heat transfer fluid	25
2.3.3	Solar tracking.....	27
2.3.4	Optical efficiency	28
2.3.4.1	Peak optical efficiency	28
2.3.4.2	Incidence angle modifier.....	28
2.3.4.3	Mutual shading factor.....	28
2.3.4.4	End loss factor.....	29
2.3.4.5	Cleanliness factor	29
2.4	SOLAR FIELD	29
2.5	THERMAL ENERGY STORAGE	30
2.6	POWER BLOCK.....	31
2.7	Performance evaluation	33
3	MODELING.....	34
3.1	PLANT CONCEPT	34
3.2	PLANT GEOGRAPHICAL LOCATION	35
3.3	METEOROLOGICAL DATA	36
3.4	THE SIMULATION ALGORITHM.....	36
3.5	SOLAR FIELD	37
3.5.1	Solar field sizing.....	39
3.5.2	Meteorological data resampling.....	39
3.5.3	Solar tracking.....	40
3.5.4	Optical efficiency	41
3.5.4.1	Incidence angle modifier.....	41
3.5.4.2	Mutual shading.....	41
3.5.4.3	End loss	41
3.5.4.4	Cleanliness factor	42
3.5.5	Solar field absorbed energy	42
3.5.6	Nodal energy balance	44
3.5.7	Heat transfer fluid freezing protection.....	46
3.5.8	Mass flow rate controller	46

3.5.9	Collector defocusing	47
3.5.10	Solar field nominal parameters	48
3.6	THERMAL ENERGY STORAGE	48
3.6.1	Storage tank sizing	48
3.6.2	Hot tank mass and energy balances.....	50
3.6.3	Cold tank mass and energy balances	50
3.6.4	Tank heat loss	51
3.6.5	Tank temperature control.....	51
3.6.6	Thermal energy storage nominal parameters.....	52
3.7	POWER BLOCK	52
3.7.2	The modeled Rankine cycle	53
3.7.3	Plant net electrical power output definition.....	53
3.7.4	Power block nominal parameters	54
3.8	SIMULATION INITIAL CONDITIONS	56
3.9	OPERATION MODEL.....	56
4	RESULTS AND DISCUSSION	58
3.10	ANNUAL PERFORMANCE	58
3.11	MODEL VALIDITY CHECK.....	63
5	CONCLUSION	66
6	FUTURE WORK SUGGESTION	67
	REFERENCES	Error! Bookmark not defined.
	APPENDIX A – MOLTEN SALT AND AIR THERMODYNAMIC PROPERTIES.....	73
	APPENDIX B – HCE THERMAL RESISTANCES.....	74
B.1	CONDUCTION BETWEEN THE HTF AND THE ABSORBER TUBE.....	74
B.2	CONDUCTION THROUGH THE ABSORBER TUBE	75
B.3	RADIATION BETWEEN THE ABSORBER TUBE AND THE GLASS ENVELOPE	75
B.4	CONDUCTION THROUGH THE GLASS ENVELOPE	76
B.5	CONVECTION BETWEEN THE GLASS ENVELOPE AND THE ENVIRONMENT	76
B.6	RADIATION BETWEEN THE GLASS ENVELOPE AND THE ENVIRONMENT 77	
	APPENDIX C – Power block Physical model.....	78
C.1	TURBINES	78
C.2	GROSS TO NET CONVERSION.....	78
C.3	CONDENSER	79
C.4	PUMPS	79

C.5	MIXING VESSELS AND DEAERATOR.....	79
C.6	MOLTEN SALT HEAT EXCHANGERS	80
C.7	CYCLE EFFICIENCY	81
C.8	DESIGN PARAMETERS	81

1 INTRODUCTION

Renewable energy sources are a topic of increasing interest all over the world. Whether for economic-strategic reasons, such as reducing energy dependence on fossil fuels or for environmental reasons such as global warming caused by excessive emissions of greenhouse gases, investment in these sources of energy has been expanding.

The sun as a source of renewable energy is a crucial element in the future of the global energy matrix given the amount of energy that this source provides. According to Chen (2011), the solar radiation incident on Earth in one year would be sufficient to supply ten thousand times the global energy demand in 2007.

One way to use the sun as a source of renewable energy is to capture the heat generated by the absorption of solar radiation (DESIDERI et al., 2013). Concentrated solar power (CSP) plants are power stations that use this radiation to thermal conversion process to generate electricity. At these systems, the solar radiation might be concentrated and focused on a heat collection element (HCE) using four different concentration technologies: parabolic trough, solar tower, Fresnel collectors and parabolic disc (IEA, 2014). In HCE, the radiant energy is absorbed and transferred to a heat transfer fluid (HTF). The fluid, in turn, transports the thermal energy to a thermal engine that transforms it into mechanical energy that soon after is converted to electricity (BLANCO, MILLER, 2017).

The energy absorbed on the HCE might also be stored in thermal energy storage (TES) system for later usage, in periods low or no insolation. An energy storage system is a desirable component in renewable energy sources since it gives stability and flexibility to the energy generation. In the case of CSP plants, storing thermal energy is an even better advantage since storing heat is much easier and cheaper than directly storing electricity (HERRMANN, KEARNEY, 2002).

Despite the advantages of being a renewable energy source with stable power generation, CSP technology does not have the same economic feasibility of other renewable sources such as wind and hydraulic, widely applied in the production of electricity on a large scale (WAGNER, 2008). In order to make this technology more competitive, studies such as those carried out by Kearney et al. (2003) have proposed increasing the efficiency of CSP plants through the use of alternative heat transfer fluids. Among these fluids, one of the most prominent was the molten salts since they work in higher temperature ranges than the synthetic oil commonly used in CSP plants already in operation around the world.

If in the global scenario the CSP technology is still consolidating, in Brazil it is incipient. Even with optimal solar resources for solar thermal applications, with locations such as the

semi-arid Northeast with normal direct irradiance above 2000 W/m²/year (GUIMARÃES et al., 2010), only two test projects to be implemented in the country are known. The first is the pilot project for a 1 MW parabolic trough plant located in Petrolina-PE (VIEIRA et al., 2012) and the second is the project for the installation of 2 solar pylons with a capacity of 100 kW each in Pirassununga-SP, and Caiçara do Rio do Vento -RN (GREEN, 30 Nov. 2018).

In addition to the solar thermal power generation potential, the introduction and consolidation of new sources in the Brazilian energy matrix is a significant topic since, as, in 2017, 65.2% of the country's electricity was generated by hydroelectric plants (EPE). The concentration of the energy production on hydraulic power makes the country highly dependent on the rain regimes and susceptible to energy shortage in case of draughts.

Thus, considering the described scenario and the scarce literature on analyzes and applications of CSP plants with advanced designs in Brazil, the present work deals with the modeling and simulation of a CSP parabolic trough plant with molten salt as a transfer fluid. It evaluates the electric power generation potential of Bom Jesus da Lapa (BA), located in the semi-arid northeast of Brazil, next to the São Francisco River. The research, therefore, started from the hypothesis that, for the chosen locality, it would be possible to generate stable solar thermal energy on a large scale.

1.1 OBJECTIVE

1.1.2 General objective

The general objective of this work is to develop a model for a concentrated solar power plant that uses parabolic trough concentration technology and molten salt as heat transfer fluid to evaluate the annual performance of this plant for allocation in Brazil.

1.1.3 Specific objectives

The specific objectives outlined were:

- To develop a simulation model for the solar field, as well as for the thermal storage system and the power block;
- To define a model of operation for the solar thermal plant;
- To determine the thermal energy output and thermal efficiency of the solar field for the typical year;
- To compute the plant's annual and monthly net electric power output, the capacity factor, and the solar-electric efficiency;

In order to achieve the general and specific objectives of the research, it was decided to implement the model of the plant using MATLAB and Engineering Equation Solver (EES) software, as well as to perform the simulation of its operation with typical meteorological data across the period of one year. In order to verify the plausibility of the implemented models and the results obtained from the executed simulation, a comparison was made between these results and those computed in simulation in the System Advisor Model (SAM) program.

1.2 STRUCTURE OF DOCUMENT

Besides the introductory chapter, this work is composed of other five chapters that address the research subject as follows: Chapter 2 addresses a background review on the CSP electricity generation technology. In this chapter, the main components of a concentrated solar power plant are described. Chapter 3 summarizes the performance model for the different components and the plant's operation model. Chapter 4 present the simulation results the simulation results for the chosen location in Brazil. Finally, chapters 5 and 6 present some conclusion derived from the simulated model and its results and suggestions for future works, respectively.

2 BACKGROUND

This chapter deals with describing and outlining the background information necessary to understand and contextualize the functioning of a CSP plant with parabolic trough technology, and that uses molten salt as HTF. The description follows the energy conversion flux by starting with the solar energy, passing through the concept of concentrated solar power plants and briefly outlining the plant's different components and their characteristics and finally defining some plant performance parameters.

2.1 SOLAR ENERGY

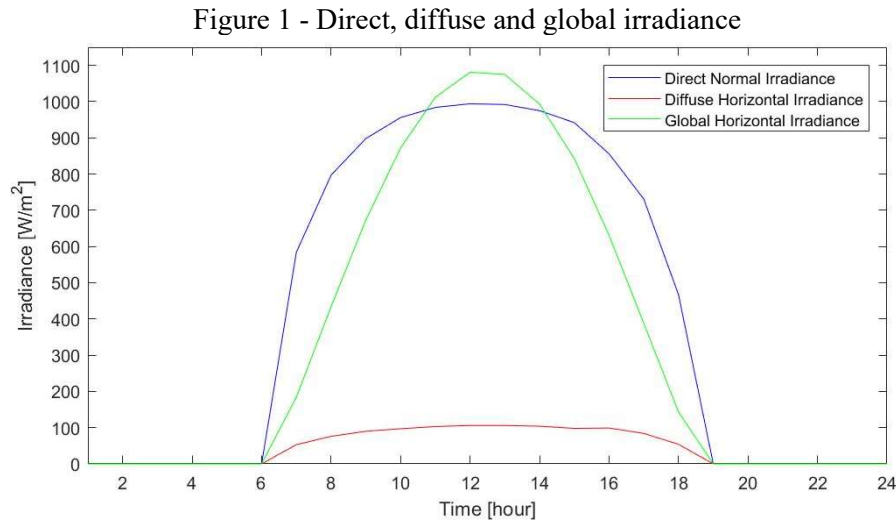
When observed from Earth, the sun behaves as a black body with a temperature of 5777K. With measurements taken for over a century, the solar radiation intensity value measured just outside of Earth's atmosphere and for a mean Earth-Sun distance found has the value of 1367W/m^2 . During the measurement period this intensity varied no more than 0.1%, and therefore it was given the name of Solar Constant (DUFFIE, BECKMAN, 2006).

Besides the magnitude, another essential characteristic of the solar radiation flux is its propagation direction and how it interacts with Earth's atmosphere. While still in space, all radiation coming from the sun has a straight and ordered propagation direction. After reaching Earth's atmosphere and interacting with its molecules and particles, the radiation might get dispersed by going through the reflection, diffusion and absorption phenomena.

The incoming radiation that arrives on Earth's surface can be divided into three different types: direct, diffuse and global radiation. The direct radiation is the portion of the radiation that hasn't been dispersed by the atmosphere and still preserves its beam ordered propagation. Consequently, direct radiation is more present in clear sky days, in which there is a reduced quantity of particles in the atmosphere, and can be concentrated. The diffuse radiation is the portion of the radiation flux that interacted with the atmosphere and got scattered in all directions. As interaction is needed, the higher the number of molecules present in the sky, the higher the diffuse percentage of the incoming radiation. Therefore, diffuse radiation prevails on cloudy days. The global radiation is the sum of both direct and diffuse radiations (DUFFIE, BECKMAN, 2006).

Irradiance is another crucial concept related to solar energy. By definition, irradiance is the rate in which radiant energy is incident on a surface per unit area - W/m^2 - (DUFFIE, BECKMAN, 2006). When the irradiance takes into account the direct solar radiation that is perpendicularly incident in a plane on Earth's surface, it is called Direct Normal Irradiance

(DNI). Figure 1 shows the irradiance levels for the direct, diffuse and global radiations for a typical clear sky summer day.



Source: Own authorship.

2.2 CONCENTRATED SOLAR POWER SYSTEMS

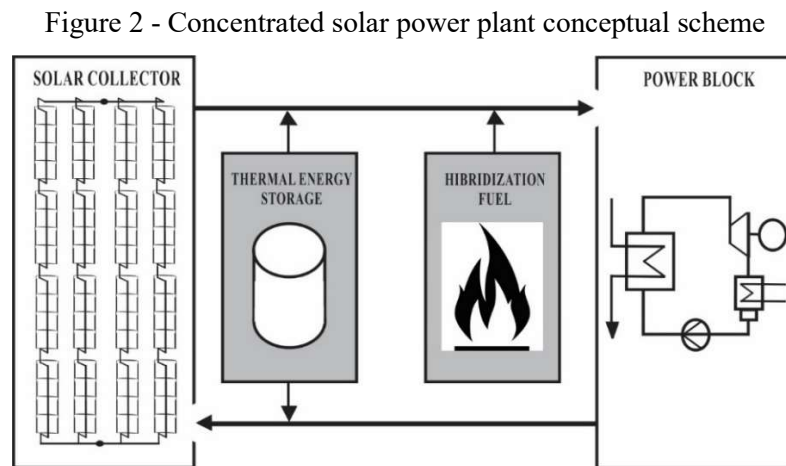
The solar energy can be converted into electric power through the photovoltaic process or thermodynamic cycles (DESIDERI et al., 2013). In the first conversion route, electricity is obtained with the use of components made of semiconductor materials. These materials, between which silicon is the most used, absorb the solar radiation and release part of the absorbed energy as electric current (GREEN, 2002). The second method of energy conversion uses thermosolar energy, heat produced by the absorption of solar radiation, to power heat engines and turn thermos energy into mechanical power used afterward to generate electricity (DUFFIE, BECKMAN, 2006).

Thermo solar energy can be collected using flat-plate or concentrating collectors. Systems that use concentrating collectors are called Concentrated Solar Thermal (CST) systems. These systems can be used to generate heat with low temperature for applications such as housing heating or can be used to generate heat with high temperatures for an application like industrial processing. Concentrated Solar Power plants are large CST systems that generate heat at high temperatures and uses this heat to generate electric energy (BLANCO, MILLER, 2017).

Conceptually, a CSP plant is composed of two interconnected circuits, figure 2. The first circuit is called a solar field. The Solar Field is composed of many parallel rows of sun-tracking concentrating collectors in which incident radiant energy is harnessed by heating a Heat Transfer Fluid (HTF) that flows through it (BARLEV, VIDU, STROEVE, 2011). The second

CSP plant circuit is a heat engine that converts the thermal energy to mechanical typically through a Rankine cycle (VALLENTIN, VIEBAHN, 2010). This conversion starts by directing the heated high-temperature HTF to a train of heat exchangers where superheated steam is produced to feed to a steam turbine. After the steam turbine, the steam is condensed into water by a heat sink and routed back to the train of heat exchangers.

The Solar Field concentration technology and HTF may vary depending on the plant application and power output. For example, water can be used as HTF to directly generate steam in the Solar Field in what is called Direct Steam Generation (DSG) (THOMAS, 1996). The Solar Field may or may not have an energy storage system, also known as Thermal Energy Storage. Another possible feature to the Solar Field is hybridization with fossil fuels that could be used for auxiliary HTF heating or back-up system (BLANCO, MILLER, 2017).



Source: Own authorship.

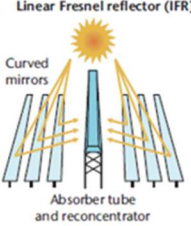
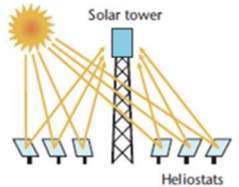
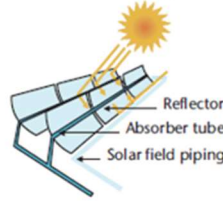
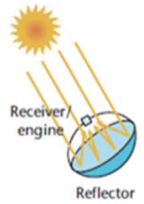
2.2.1 Solar concentration technologies

A solar collector is a heat-exchanging apparatus that can transform solar to thermal energy. These collectors can be stationary and non-concentrating, usually flat-plate collectors, or sun-tracking and concentrating collectors. Concentrating collectors use optical elements, like mirrors and lens, to focus large amounts of radiation onto a small receiving device while following the sun through its course to maximize solar flux at their focus (BARLEV, VIDU, STROEVE, 2011).

There are four main types of concentrating collector technologies: the parabolic trough collector (PTC), the heliostat field collector, also known as Solar Tower, the linear Fresnel reflectors and the parabolic dish collectors. These different concentration technologies can be categorized by their focus region and by their receiver's mobility, figure 3 (IEA, 2014).

Furthermore, as can be seen in the comparative summary in Table 1, the different technologies can achieve different concentration ratios and therefore can operate in different temperature ranges.

Figure 3 - Concentration technologies classification chart

Focus type Receiver type	Line focus Collectors track the sun along a single axis and focus irradiance on a linear receiver. This makes tracking the sun simpler.	Point focus Collectors track the sun along two axes and focus the irradiance at a single point receiver. This allows for good receiver efficiency at higher temperatures.
Fixed Fixed receivers are stationary devices that remain independent of the plant's focusing device. This eases the transport of collected heat to the power block.	Linear Fresnel reflector (IFR) 	Central receiver 
Mobile Mobile receivers move together with the focusing device. In both line focus and point focus designs, mobile receivers collect more energy.	Parabolic trough 	Parabolic dish 

Source: Adapted from IEA (2014).

The parabolic trough collectors are the most mature CSP technology, and therefore it is the most used even though it has the disadvantage of occupying a large area to function. Parabolic trough collectors have been used in micro applications since 1870, but it was only after the oil crisis in the 1970s that solar energy is drawn international attention as an alternative energy source and led to the development of various parabolic trough systems. The parabolic trough reached its maximum maturity in the United States with the development of the SEGS (Solar Electric Generating Systems) plants in the Mojave Desert in California (FERNÁNDEZ-GARCÍA et al., 2010). Nowadays, due to its technological maturity, the application of PTC has expanded and is being used in different power production settings such as hybridized plants. For example, parabolic trough technology can be used for auxiliary heating to sugarcane cogeneration plants (BURIN, 2015).

Table 1 - CSP technologies characteristics

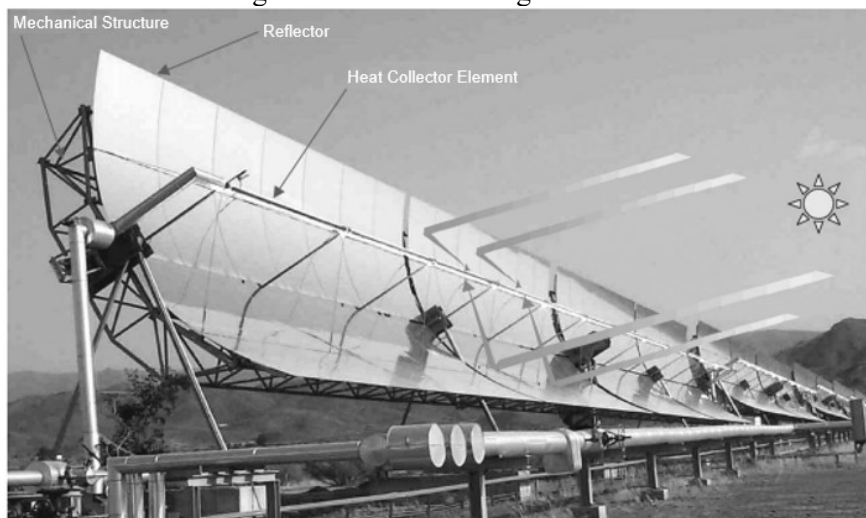
Collector Type	Relative Thermodynamic Efficiency	Relative cost	Concentration ratio (sun)	Technology maturity
Parabolic Trough	Low	Low	15-45	Very Mature
Linear Fresnel	Low	Very Low	10-40	Mature
Solar Tower	High	High	150-1500	Most Recent
Parabolic Dish	High	Very High	100-1000	Recent

Source: Adapted from Barlev, Vidu, Stroeve (2011).

2.3 PARABOLIC TROUGH COLLECTOR

The primary component of a solar field build with parabolic trough collectors is the solar collector assembly (SCA). This assembly is composed of several parabolic reflectors and heat collector elements (HCE) lined up and bundled together by a mechanical bearing structure that englobes, as in figure 4. This mechanical structure is connected to a tracking system that moves the structure and align the collector's reflective surface to the sun. (SÁ, 2013). In commercial CSP applications, the assemblies are north-south oriented in order to maximize the amount of power produced along the year (FERNÁNDEZ-GARCÍA et al., 2010).

Figure 4 - Parabolic trough collector



Source: Adapted from Price et al. (2002).

Modern collector constructions have been evolving since their introduction in the first SEGS plant. The collectors LS-1, LS-2, and LS-3 developed by the American-Israeli company LUZ improved from a model to the other as they were installed in the different SEGS units. These are called the first generation of collectors (PRICE et al., 2002). Afterward, based on the experience gained so far, the European consortium Eurotrough developed the collectors ET-100 and ET-150, known as the second generation of collectors. The main difference between these two models is their assembly length. While the first had 100 meters, the second had 150 meters of length. Commonly, four assemblies of the ET-150 collectors are used per loop. This loop set is capable of producing outlet HTF temperatures above 500 °C (GEYER et al., 2002).

These two generations of collectors built a knowledge base from which companies in Europe and the United States started to create their third-generation solar collector models aiming at objectives such as cost reduction, optimized use of molten salts as HTF, optimized mechanical bearing structure to weight and structural deformation reduction and aperture area increase (FERNÁNDEZ-GARCÍA et al., 2010). The German company Flabsol GmbH developed the SKAL-ET, the third generation Eurotrough collector, from minor modifications in the previous versions for solar field cost reduction (SCHIEL et al., 2006). The Italian National Agency for New Technologies, Energy and Sustainable Economic Development (ENEA) and the Ronda Group designed their Ronda RHT 2500 collector focusing on the use of molten salt as HTF (WAGNER, 2013). Its dimensions are slightly larger than the Eurotrough's ones. On the other hand, the Spanish company SENER opted for optimizing the bearing structure for manufacture cost reduction (CASTAÑEDA, VAZQUEZ, DOMINGO, 2006).

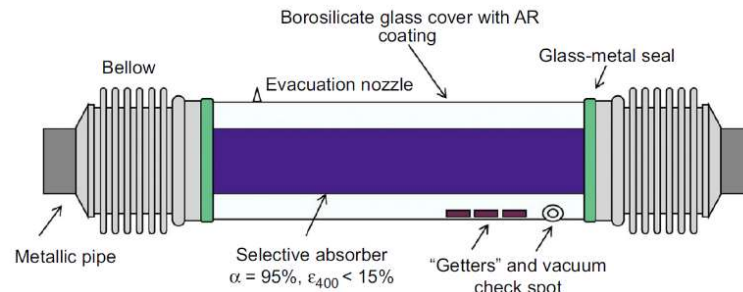
More recently, collector designs have focused on enlarging the heat collected in the assemblies by enlarging the collector size and aperture area. The third generation Ultimate trough, from the German company Flabeg GmbH, follow this guideline (SCHWEITZER et al., 2011). Leaning towards higher power output justifies itself financially due to the economy of scale (KOLB et al., 2011; RUEGAMER et al., 2014).

2.3.1 Heat collector element

The heat collector element, also called receiver, is mainly composed by an absorber tube, a glass envelope and expansion bellows, figure 5. The absorber tube is steel tube coated with a solar selective substance that has a high absorption over all the solar spectrum range and has low thermal radiation emission. The glass envelope involves the absorber tube creating a cavity that can be vacuumed minimizing, therefore, convective heat losses. The expansion

bellows allow for the absorber tube and glass envelope to dilate differently without damaging the receiver integrity (MORALES, SAN VICENTE, 2017; PRICE et al., 2002).

Figure 5 - Schematics of a shortened heat collect element



Source: Morales e San Vicente (2017).

According to (GÜNTHER, JOEMANN, CSAMBOR, 2011) there are, currently, three manufacturers of receivers: the German companies SCHOTT and Siemens and the Italian company Archimede Solar Energy. By being used in many of the existing plants in operation, like the Andasol I, II and III solar thermal power plants, the receiver SCHOTT PTR70 must be highlighted as the state-of-the-art of PTC receivers (WAGNER, 2013). SCHOTT produce other models of receivers such the PTR80 and the PTR90, and the difference between these three models is their absorber outer diameter size, 70, 80 and 90 millimeters respectively (Wagner, 2013). All these models use synthetic thermal oil as HTF and are designed to an operating temperature of 400°C . Not long ago, SCHOTT presented the PTR70 Advanced. Supposedly, it is an optimized version of the original PTR70 that uses molten salt as HTF however little technical information could be found about this receiver model (SCHOTT Solar CSP, 2013).

Starting in the opposite direction with a design focused, since the beginning, on the use of molten salt, the Archimede developed HMES-8 receptor. Currently, their most advanced receiver for molten salt is the HCEMS-11 with an operating temperature of 550°C (MACCARI et al., 2015).

2.3.2 Heat transfer fluid

The organic eutectic mixture Biphenyl-diphenyl-oxide known commercially as Therminol VP-1 or Dowtherm A is the state-of-the-art HTF for PTC power plants. The advantages of this HTF is its low freezing point of 12°C and its low corrosivity (RAADE, PADOWITZ, 2011). However, it has many limiting disadvantages like a maximum operating temperature of 400°C , after which the oil suffers from thermal degradation, high toxicity, making leaks environmentally hazardous, high vapor pressure, meaning that it evaporates

easily, therefore, making it not suitable to be stored, and finally, it is relatively expensive fluid, as can be seen in table 2.

Many strategies to counter and solve the synthetic oil disadvantages are being studied. One of these strategies is using alternative fluids as HTF. According to Moya (2017a), the leading alternatives are water, for Direct Steam Generation (DSG), pressurized gasses, like CO₂ and N₂, and molten salts. Among these solutions, the molten salt is distinguished by the fact that it can work at temperatures above 500 ° C and because this material can be used as both HTF and energy storage medium.

After research made by the American *Sandia National Laboratories* and *National Renewable Energy Laboratory* (NREL) on different possible salts for CSP usage, nitrate salts were proven as the best option due to corrosion and cost characteristics (GUILLOT et al., 2012). These salts have high thermal stability, high density, high heat capacity, good thermal and electric conductivity, relatively low viscosity and low vapor pressure. Commercially there are 3 different mixtures available: Solar Salt (60% *NaNO₃*/40% *KNO₃*), the Hitec (7% *NaNO₃*/53% *KNO₃*/40% *NaNO₂*) and the Hitec XL (7% *NaNO₃*/45% *KNO₃*/48% *Ca(NO₃)₂*) (KEARNEY et al., 2003).

Table 2 - Operation temperature and cost comparison between the heat transfer fluid Solar Salt, Hitec Salt, Hitec XL Salt, and the Therminol VP-1

Parameter	Solar Salt¹	Hitec¹	Hitec XL¹	Therminol VP-1¹
Freezing Temperature [°C]	220	142	120	12
Maximum Operation Temperature [°C]	600	535	500	400
Nominal Cost [USD/kg]	0.49	0.93	1.19	2.2

Source: Adapted from Kearney et al. (2003).

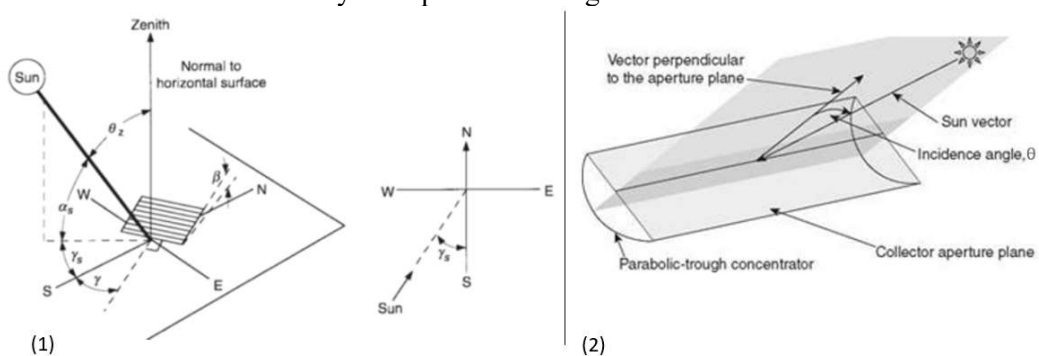
It is important to notice that the molten salts have a high freezing temperature which means that special attention must be given for the temperature fluctuations in the system. The molten salt has to be maintained liquid since small solidified pieces of salt can cause severe damage to different plant components such as pumps (KEARNEY et al., 2004). To control the freezing two different methods are used: impedance heating and mineral insulated heat tracing (PACHECO, KOLB, 1997). Furthermore, it is noticeable that the commercial CSP plants in operation running with molten salt as HTF are all solar tower plants, choose using Solar Salt, despite its relative higher freezing temperature, because it is cheaper since in these enterprises the salt inventory is the most expensive part (MOYA, 2017a; STEINMANN, 2014).

2.3.3 Solar tracking

Tracking the sun's movements across the sky, and moving the collectors accordingly, can maximize the energy collected by the solar field. The geometric relationships between a plane of any particular orientation relative to the Earth at any time and the incoming direct solar radiation, that is, the position of the sun relative to that plane, can be described regarding some angles, figure 6. According to Duffie e Beckman (2006), the main angles to characterize this sun-plane position relationship and the sun's position in the sky for a parabolic trough collector are:

- Latitude (ϕ) - The latitude is the angular location north or south of the equator (north positive);
- Declination (δ) - the angular position of the sun at solar noon with respect to the plane of the equator;
- Hour Angle (ω) – The angular displacement of the sun east or west of the local meridian due to rotation of the earth on its axis at 15° per hour (morning negative and afternoon negative);
- Solar Zenith Angle (θ_z) - The angle between the vertical axis and the line to the sun, that is, the angle of incidence of the direct radiation on a horizontal surface;
- Angle of Incidence (θ) - The angle between the beam radiation on the surface and the normal to the surface;

Figure 6 - Main angles to characterize this sun-plane position relationship and the sun's position in the sky for a parabolic trough collector



Source: Adapted from Duffie e Beckman (2006) and Moya (2012b).

Besides positioning, tracking deals with timing. A specific type of time is used for solar applications. Solar time is a time base that represents the apparent angular motion of the sun across the sky. This time base does not coincide with the local clock time. It is necessary to apply correction factors shown in section 3.5.3 to convert standard time to solar time. Also,

solar noon always happens when the sun crosses the observer's meridian (DUFFIE, BECKMAN, 2006).

2.3.4 Optical efficiency

The Optical Efficiency (η_{opt}) of a parabolic trough collector in a CSP plant solar field is the rate between the radiant energy available at the HCE's absorber tubes for HTF heating and the incident DNI. A myriad of factors can influence this energy conversion efficiency. The main efficiency reduction factors can be associated with the collector's single axis solar tracking, with the collector's constructive aspects or with the interaction between collectors. Taking these factors in account, the optical efficiency for a parabolic trough solar field can be calculated by equation 2.1.

$$\eta_{opt} = \eta_{opt,0^\circ} \cdot \eta_{IAM} \cdot \eta_{Shadow} \cdot \eta_{EndLoss} \cdot \eta_{clean} \quad (2.1)$$

2.3.4.1 Peak optical efficiency

The Peak Optical Efficiency ($\eta_{opt,0^\circ}$) is the optical efficiency found when the incomings solar radiation is normal to the reflector's aperture area and, the incidence angle is equal to zero. Consequently, the peak optical efficiency is the maximum efficiency reached by a parabolic trough collector. This efficiency, taking into consideration physical characteristics from the HCE and reflector, is composed, as shown in equation 2.2, by the reflector reflectivity (ψ), the transmissivity of the HCE's glass envelope (τ_{env}) and the absorptivity of the absorption tube (α_{env}). The final component is the Intercept Factor (γ_θ) that accounts microscopic and macroscopic errors that don't depend on the relative position of the sun such as ripples on the reflecting surface (ECK et al., 2014; MOYA, 2012b).

$$\eta_{opt,0^\circ} = \psi \cdot \alpha_{abs} \cdot \tau_{env} \cdot \gamma_\theta \quad (2.2)$$

2.3.4.2 Incidence angle modifier

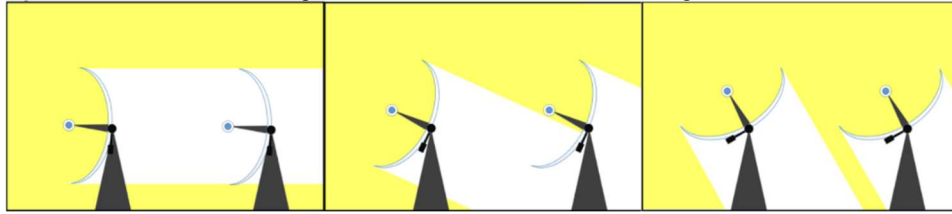
The Incidence Angle Modifier (η_{IAM}) is a correction factor associated with the losses generated by that fact that the radiation is incident in the collectors with a certain inclination, identified as the incidence angle. For example, HCE and reflectors optical properties varies with the incidence angle (ECK et al., 2014).

2.3.4.3 Mutual shading factor

The mutual shading factor (η_{Shadow}) is the derate factor that accounts for the losses caused by total or partial shadowing between consecutive rows due to collector tracking

position, as can be seen in figure 7. The shadowing phenomenon happens in the beginning of the mornings and at the end of the afternoons (ECK et al., 2014).

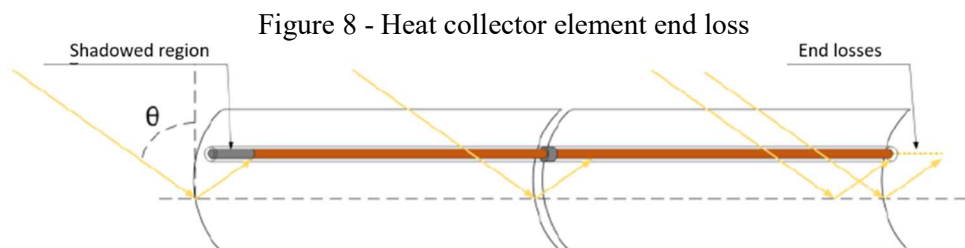
Figure 7 - Collector mutual shading



Source: Sá (2013).

2.3.4.4 End loss factor

The end loss factor ($\eta_{EndLoss}$) is a correction factor that accounts for the radiation losses in the longitudinal direction due to the inclination of the solar radiation. Depending on the incidence angle, no solar radiation may arrive at the beginning of the collector's HCE, creating a shadowed region, at the same time that the radiation arriving at the end of the collector is being reflected out and lost, as shown in figure 8 (ECK et al., 2014).



Source: Sá (2013).

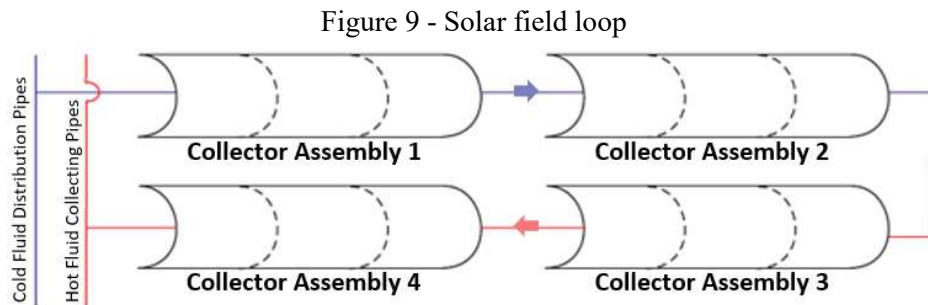
2.3.4.5 Cleanliness factor

The cleanliness factor (η_{Clean}) is a constant derate to the optical efficiency that represents reflectivity reduction in the collector assemblies' reflectors due to dirt accumulation (WAGNER, 2013).

2.4 SOLAR FIELD

On a system level, the solar field is composed of loops. Solar field loops are formed by two or more consecutive solar field rows connected in series while the rows are formed by many collector assemblies connected in series in the same line, figure 9. During the day, all HTF heating process happens inside a loop, usually made of a pair of rows. The fluid enters the loop on its cold state and rises in temperature as it passes through the assemblies reaching its maximum temperature at the outlet of the last assembly (BLANCO, MILLER, 2017).

At night, the solar field may or may not have fluid circulating through it depending on the HTF used. As synthetic oil, like the Therminol, have low freezing temperature they can be kept stationed in the solar field through the night. Molten salts with their high freezing temperature have to be kept circulating in the solar field all night (KEARNEY et al., 2004).



Source: Own authorship.

Depending on the thermal energy demanded to generate the electricity and to store for later hours, the solar field may have different sizes and different layouts. When sizing the solar field, it is essential to consider the two demands. If the TES is present, the solar field outlet heat must be sufficient to cover for the power block needs and to charge the storage. The Solar Multiple is the ratio represents this sizing consideration.

According to Montes et al. (2009), it can be defined as the ratio between thermal power generated by the solar field at nominal conditions and the thermal power required to run the power block at nominal conditions. The larger the solar multiple, the larger the solar field size. As the solar field is the costliest part of a CSP plant, the solar multiple is usually optimized in a way that minimizes the LCOE (QUASCHNING, KISTNER, ORTMANN, 2002).

2.5 THERMAL ENERGY STORAGE

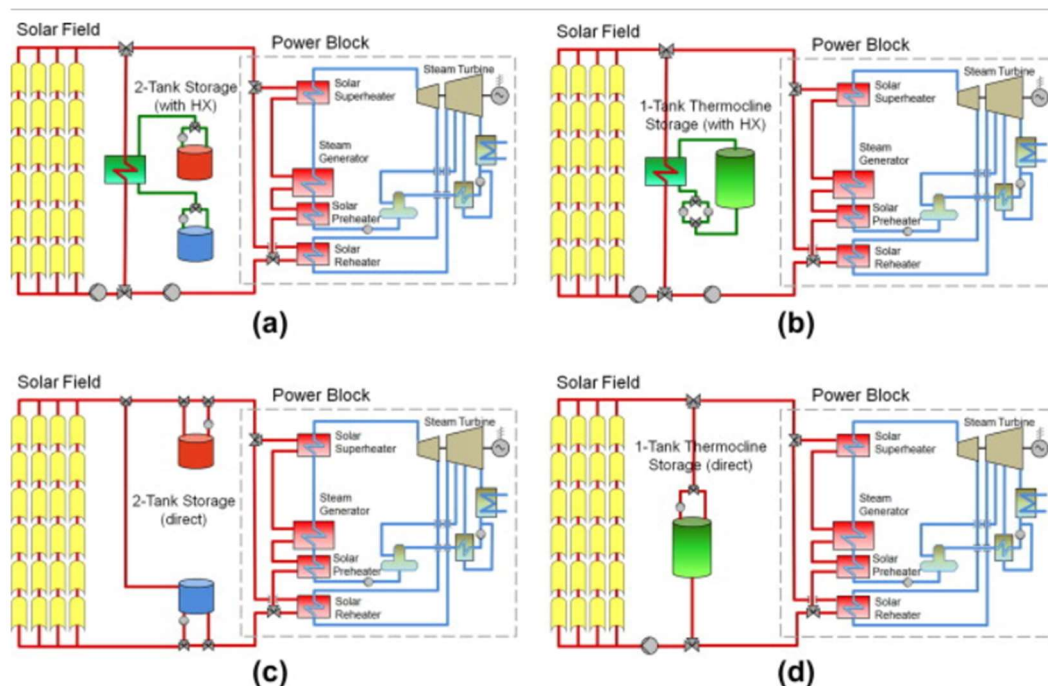
The integration of thermal energy storage systems to a CSP plant gives the plant many strategic advantages. This combination makes a CSP plant a renewable energy source not only with high dispatchability but also with high stability (DOMINGUEZ, BARINGO, CONEJO, 2012). Depending on the level of intermittence of the solar insolation, TES systems can be used for buffering (help mitigating short weather fluctuations and keeping the solar field's thermal inertia), for power delivery period displacement or extension (matching power grid demands) and for increasing the net amount of energy produced (HERRMANN, KEARNEY, 2002).

Thermal energy can store through sensible heat, latent heat or reversible endothermic chemical reactions in processes that involve charging, storing and discharging. The main TES systems are the sensible storage systems and the latent storage systems. Sensible systems use as storage means the energy that can be absorbed or released by a substance in the variation of

its internal energy and temperature without phase-change. On the other hand, latent systems use as means of storing the energy absorbed or released during a substance's phase change. While sensible heat storage can be made by liquid media (mineral oils, synthetic oil, and molten salts) or solid media (high-temperature concrete and castable ceramics used in packed beds), latent heat storage is made almost isothermally in phase change materials (PCM) that usually undergo solid-liquid transitions (GIL et al., 2010).

High-temperature thermal energy storage concepts can be divided into active and passive. Active storage systems are characterized by forced convection heat transfer into the storage material (in a solar collector or other heat exchangers). The active systems can use one or two tanks. The one tank system is also known as thermocline tank. Furthermore, active storages can be divided into direct and indirect systems. In the direct systems the HTF is also the storage medium and in the indirect system a second medium, different from the HTF, is used for storing heat (GIL et al., 2010). An example of CSP plants with direct and indirect two tank and thermocline tank arrangements can be seen in figure 10.

Figure 10 - Active storage arrangements: a - indirect two-tank, b – indirect thermocline, c – direct two-tank and d – direct thermocline



Source: Biencinto et al. (2014).

2.6 POWER BLOCK

The power block is the system that converts heat into electricity. As of 2016, this heat conversion in CSP plants is made by subcritical steam Rankine cycles (BESARATI, GOSWAMI, 2017). Besides the four essential components (boiler, turbine, heat sink and pump),

these cycles can present many other features like reheating or condensate heating through turbine extractions (SÁ, 2013). It is important to note that as CSP technology requires low cloudiness, CSP plants are commonly located on desert areas and therefore may need to rely on dry air-based cooling for the heat sink in contrast to the usual wet cooling of a cooling tower (HOOMAN, GUAN, GURGENCI, 2017).

Furthermore, one of the ways to make CSP plants more economically viable is to make the power block more efficient. As the next generation of solar thermal power plants get larger and get to work at higher temperatures, new power block configurations with higher efficiency might be used. Among these new configurations, supercritical steam Rankine cycles, air, and helium Brayton cycles, and supercritical carbon dioxide power cycles, as well as subcritical and supercritical organic Rankine cycle combination, are the candidates with the most potential (BESARATI, GOSWAMI, 2017).

2.7 PERFORMANCE EVALUATION

In general, solar thermal plants can be evaluated through the analysis of parameters such as capacity factor and solar electric efficiency. According to Madaeni, Sioshansi, Denholm (2011), the capacity factor is a parameter that measures the amount of energy that is produced by a plant and its maximum output. This parameter can be calculated by dividing the total energy produced in a year by the energy it would have produced by running all hours of the year at full load. On the other hand, the solar-electric efficiency is the parameter that indicates how much of the available incident radiant energy is transformed into electrical energy.

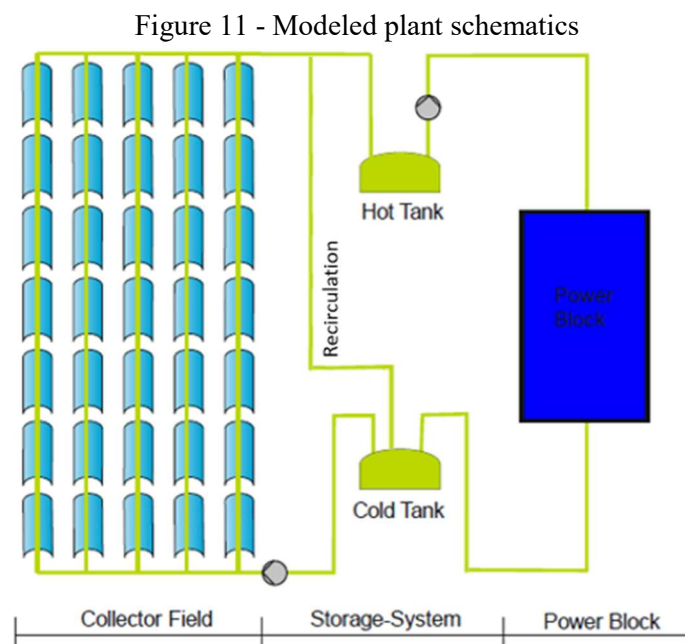
3 MODELING

This chapter addresses the description of the different models that compose the functioning of a concentrated solar power plant with parabolic trough collectors and molten salt as heat transfer fluid. The physical models of plant components are addressed first. Then, later, the operation model is described.

3.1 PLANT CONCEPT

The full plant concept modeled in this work consists of a molten salt based solar-only CSP plant composed of a solar field with parabolic trough concentrators, a direct two-tank thermal storage, and subcritical steam Rankine cycle power block, as illustrated by figure 11. As the focus of this study, using molten salt as both solar field heat transfer fluid and storage medium was chosen for its capacity of rising the power plant working temperatures and, consequently, efficiency. The use of molten salt as HTF requires the use of direct storage. The two-tank configuration was chosen because it is the most common configuration for CSP plants and because it is simpler to be modeled since its operation is not intrinsically dependent to the stratification phenomenon like the thermocline tanks.

No fossil fuel hybridization or any other burning auxiliary heating was used therefore characterizing the plant modeled in this work as a solar-only plant. This configuration was chosen because the location selected for the plant is too far from coal sources and natural gas distribution piping (ANP (2016)). Finally, the subcritical steam Rankine cycle was chosen for being the power block used currently on CSP plants.



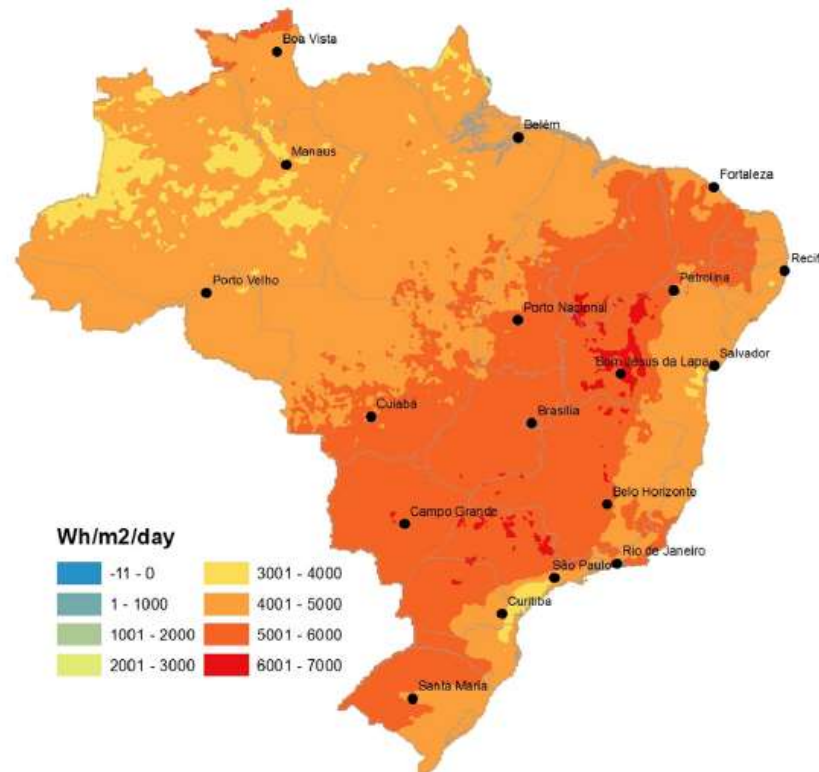
Source: Adapted from Wittmann et al. (2012).

3.2 PLANT GEOGRAPHICAL LOCATION

The selection of a location for a CSP plant may consider many practical aspects. The yearly accumulated direct normal insolation (solar radiant energy per unit area) is unquestionably the primary decision factor. The minimum level of insolation recommended for CSP enterprises most frequently cited in the literature is 2000 kWh/m²/year, or 5,5 kWh/m²/day (MALAGUETA et al., 2013). As can be seen in figure 13, Brazil has an extensive area of its territory with direct normal insolation above this minimum value.

The semi-arid region of the Brazilian Northeast is one of the areas with irradiance above the recommended levels mentioned before. On her work, Guimarães et al. (2010) analyzed multiple locations in the semi-arid region and evaluated which locations are best suited for implementing a CSP plant. The conclusion found was that the cities of Petrolina (PE), Bom Jesus da Lapa (BA) and Juazeiro (BA) were the most suitable places for such implementation. Besides the necessary irradiance level with low annual variation, these cities dispose of access to the electrical grid, to roads and airports and water, being beside one of Brazil's largest rivers, the São Francisco river. Bom Jesus da Lapa (BJL) was also chosen as the location to be used in this work because the meteorological data for this location is available. A summary of the geographical data of BJL can be seen in Table 3.

Figure 12 - Direct Normal Irradiance (DNI) distribution in Brazil



Source: Malagueta et al. (2013).

Table 3 - Geographic coordinates of Bom Jesus da Lapa

Standard longitude (λ_{std})	Local longitude (λ_{loc})	Local latitude (ϕ)
- 45°	- 43.26°	- 13.27°

3.3 METEOROLOGICAL DATA

The meteorological data (DNI, ambient dry bulb temperature and ambient wind speed) used in this work comes from the NREL National Radiation Database (NSRDB). This radiation database is considered the best source of solar data for locations like United States, Canada, Central and northern South America, Sri Lanka, India, Nepal, Bhutan, Bangladesh, and parts of Pakistan, Afghanistan, and Myanmar, and western Southeast Asia (WILCOX, 2012).

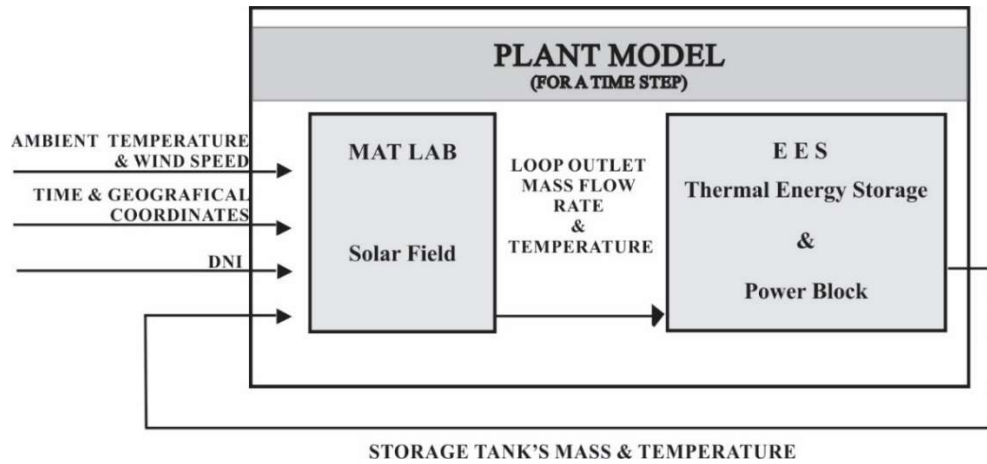
Typical-year data, also known as TMY – Typical Meteorological Year, was chosen for the simulation. A TMY file contains one year of hourly data that represents historical weather data throughout multiple years. This kind of weather file is used for simulations in which the estimate results represent an average yearly performance for a long-term solar project. (WILCOX, 2012). The TMY data from Bom Jesus da Lapa was built from the meteorological data over the 1998-2016 period.

3.4 THE SIMULATION ALGORITHM

The proposed plant model was developed using the software *MATLAB* and *Engineering Equation Solver* (EES). The simulation of the model happened for time steps of 1 hour. While all mass and energy calculations for the solar field were made into *MATLAB* for a time step, the mass and energy balances for the storage tanks were performed in EES. Also, as will be shown in section 3.7, the model for the power block was developed using *MATLAB* but integrated afterward in the storage tanks model in EES.

MATLAB was used as the main platform in which the simulation took place. In a simulation timestep, all geographic and meteorological data loaded into *MATLAB* is used in the solar field model to calculate its outlet HTF mass flow rate and temperature. Next, the model in *MATLAB* compiles the necessary input information for the storage tanks model and calls EES to solve this storage model's mass and energy balances. EES, then, exports the results back to *MATLAB* that, in turn, makes them ready for the next timestep simulation. The scheme of figure 14 illustrates this simulation process.

Figure 13 - Plant information flow schematics

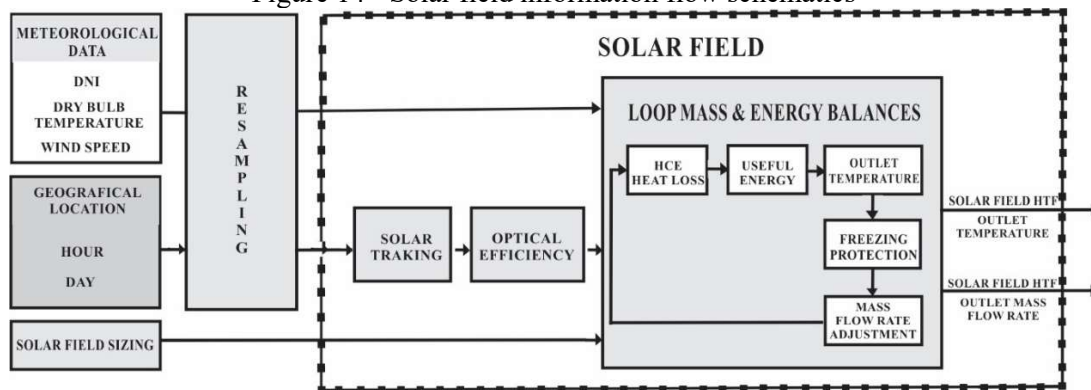


Source: Own authorship.

3.5 SOLAR FIELD

The solar field is the CSP plant system that is responsible for the conversion of solar radiant energy into thermal energy. The model developed in this work translates this process by first estimating the solar field size, estimating the solar position and the solar field collector optical efficiency for the given hour, estimating the HCE heat loss and the HTF's absorbed heat and, finally adjusting the mass flow rates to obtain the maximum loop outlet temperature possible. The meteorological data might be resampled for simulations with time steps smaller than an hour. This process schematics can be seen in figure15.

Figure 14 - Solar field information flow schematics



Source: own authorship.

The solar field collector components chosen for this work were the collector Eurotrough ET-150, with its 4 SCA per loop configuration, and the receiver HCEMS-11 from ASE. These two components were chosen because all needed technical information about them was available, Table 4 and Table 5, and because they, supposedly, fit together since the HCEMS-11 receiver has the same geometrical features of length and outer absorber diameter as the ET-150

default receiver, the SCHOTT PTR70. Lastly, the molten salt mixture selected for the plant simulation was the - 60% NaNO_3 /40% KNO_3 - Solar Salt mixture. The thermodynamic properties of the chosen molten salt, as well as of the air, can found in Appendix A.

The piping between the storage and the SCA loops at the solar field were neglected. Consequently, no pressure loss analysis was made, and no solar field molten salt pump was modeled. Furthermore, this also leads to the disregard of the thermal inertia and heat losses of the piping in the thermal balance over the solar field. The practical implementation result of this neglect is that the temperature coming out of the cold tank is used as the loop inlet temperature, and the loop outlet temperature is placed as the hot tank inlet temperature when the minimum hot tank inlet temperature is reached.

Table 4 - Main characteristic parameters of Eurotrough ET-150 solar collector

Parameter	Value	Unit
Aperture Length (L_{ap}) ¹	5.77	[m]
Focal Length (L_f) ¹	1.71	[m]
SCA Length (L_{SCA}) ¹	148.5	[m]
Net Aperture Area (A_{ap}) ¹	817.5	[m ²]
Absorber Tube Outer Diameter ($D_{abs,o}$) ¹	0.07	[m]
Reflector Mirror Reflectivity (ψ) ²	0.92	-
Intercept Factor (γ_θ) ²	0.92	-

Source: 1 - Lüpfer et al. (2003) ; 2 - Montes et al. (2009).

Table 5 - Main characteristic parameters of the HCEMS-11 receiver

Parameter	Value	Unit
Maximum Operation Temperature ¹	550	[°C]
Maximum Operation Pressure ¹	20	[bar]
Absorber Tube Outer Diameter ($D_{abs,o}$) ¹	0.07	[m]
Absorber Tube Inner Diameter ($D_{abs,i}$) ¹	0.064	[m]
Absorber Tube Absorbance (α_{abs}) ¹	0.95	-
Absorber Tube Emissivity at 400°C (ζ_{abs}) ¹	0.074	-
Absorber Tube Thermal Conductivity at 500°C (κ_{abs}) ²	22	[W/m/K]
Glass Envelope Outer Diameter ($D_{env,o}$) ¹	0.125	[m]
Glass Envelope Inner Diameter ($D_{env,i}$) ¹	0.119	[m]
Glass Envelope Absorbance (α_{env}) ³	0.02	-
Glass Envelope Emissivity (ζ_{env}) ³	0.86	-
Glass Envelope Transmissivity (τ_{env}) ¹	0.969	-
Glass Envelope Thermal Conductivity (κ_{env}) ³	1.04	[W/m/K]

Source: 1 - Archimede Solar Energy (2016); 2 - AK Steel (2012); 3 - Sá (2013).

3.5.1 Solar field sizing

To determine the size of the solar field means to calculate the number of solar field loops. This calculation is done using equation three where $P_{gross,nom}$ is the plant's nominal gross electrical power output, SM is the solar multiple, η_{PB} is the power block nominal efficiency, DNI_{nom} is the solar field's nominal DNI, $\eta_{opt,0^\circ,nom}$ is the solar field nominal optical efficiency, A_{ap} is the collector aperture area and N_{SCA} is the number of collector assemblies in the solar field loop. While the upper part of the equation accounts for the thermal energy that the solar field must deliver, the lower part accounts for the thermal energy a loop can provide on design conditions. Furthermore, the number of loops obtained with equation 3.1 is always rounded to the next larger even number since solar field usually have even distribution if loops.

According to Moya (2012b), the nominal DNI is the radiance found at noon of a summer day at the CSP plant's location. Montes et al. (2009) choose to use 21st of June – the northern hemisphere's summer solstice – to determine the nominal irradiance for his simulation. Following a similar approach to Moya (2012b) and Montes et al. (2009), the value of 963 W/m² was chosen as the nominal DNI. This value is the average between the noon irradiance on the 21st and the 22nd of December since these are the days in which the southern summer solstice can happen.

$$N_{loop} = \frac{P_{gross,nom} \cdot SM \cdot (1/\eta_{PB})}{DNI_{nom} \cdot \eta_{opt,0^\circ,dsgn} \cdot A_{ap} \cdot N_{SCA}} \quad (3.1)$$

With the model described, the determination of the solar field size relies on choosing the solar multiple value. The solar multiple chosen for the simulations performed in this work has a value of 2.

3.5.2 Meteorological data resampling

As the available TMY data is hourly based, to allow for smaller time steps this data has to be resampled. The resampling process starts by rearranging the data in a matrix with the hourly data being grouped by day. Each day data group is then interpolated and resampled for the desired time step using the *MATLAB* function *interp1* with the Shape-preserving piecewise cubic interpolation (PCHIP) method.

Even though the option to adopt smaller time increments than the original meteorological data's time steps, the simulation performed kept the time increment length of 1 hour. The choice had to do with the fact that for time steps of one hour the simulation already

took a long time to be performed, about 15 hours for a computer with processor Intel Core-i5 7200U (2.5 GHz).

3.5.3 Solar tracking

As described in section 2.3.3, solar tracking main focus is the determination of the sun's trajectory across the sky through the day. Such determination can be done by calculating the declination, the hour angle and the solar zenith angle. Afterward, the incidence angle, the angular relationship between the direct solar irradiation and the collectors, can be calculated. All equation in this section come from Duffie e Beckman (2006).

First, the declination (δ) can be escribed by the equation 3.2 where y is the day of the year, from 1 to 365.

$$\delta = 23.45 \sin\left(\frac{360 \cdot (284 - y)}{365}\right) \quad (3.2)$$

Next, to calculate the solar angle (ω), equation 3.3, it is necessary to know the solar time, in hours, which, in turn, is calculated by equation 3.4.

$$\omega = 15 \cdot (t_{sol} - 12) \quad (3.3)$$

$$t_{sol} = t_{std} + \frac{Shift}{15} + \frac{E}{60} \quad (3.4)$$

The *Shift* is calculated as the difference between the standard longitude and the local longitude, equation 3.5. The standard longitude is the longitude of the location's time zone.

$$Shift = \lambda_{std} - \lambda_{loc} \quad (3.5)$$

The solar time correction (E), in minutes, is calculated with equation 3.6 and equation 3.7.

$$E = 229.2 \cdot (7.5 \times 10^{-5} + 1.868 \times 10^{-3} \cos(B) - 3.2077 \times 10^{-2} \sin(B) - 1.4615 \times 10^{-2} \cos(2B) - 4.089 \times 10^{-2} \sin(2B)) \quad (3.6)$$

$$B = \frac{360 \cdot (y - 1)}{365} \quad (3.7)$$

Finally, the zenith angle can be calculated by equation 3.8.

$$\theta_z = \cos^{-1}(\sin(\delta) \sin(\phi) + \cos(\delta) \cos(\phi) \cos(\omega)) \quad (3.8)$$

With the values of declination, hour angle and solar zenith, calculating the incidence angle, equation 3.9. This equation represents the incidence angle for single axis tracking collectors aligned in the north-south direction with continuous adjustment to minimize the angle of incidence.

$$\cos \theta = (\cos^2(\theta_z) + \cos^2(\delta) \cdot \sin^2(\omega))^{1/2} \quad (3.9)$$

3.5.4 Optical efficiency

3.5.4.1 Incidence angle modifier

According to Geyer et al. (2002), equation 3.10 calculates the incidence angle modifier for the ET-150 solar collector.

$$\eta_{IAM} = \cos(\theta) - 2.859621 \times 10^{-5} \cdot \theta^2 - 5.25097 \times 10^{-4} \cdot \theta \quad (3.10)$$

3.5.4.2 Mutual shading

According to Wagner e Gilman (2011), the shadow loss factor can be calculated with equation 3.11. It takes into account the collector aperture length (L_{ap}), the distance between rows (L_{btw_rows}) and the position of the sun in relation to the collector with the zenith and incidence angles.

$$\eta_{Shadow} = \min \left(1, \max \left(0, \frac{L_{btw_rows} \cdot \cos(\theta_s)}{L_{ap} \cdot \cos(\theta)} \right) \right) \quad (3.11)$$

3.5.4.3 End loss

Depending on the incidence angle, the first reflected solar beams reach the HCE at a certain distance of the receiver's tip leaving a section without concentrated radiation. Similarly, depending on the incidence angle, the solar beams to reach the end of a collector assembly gets reflected without reaching that collector's HCE. However, part of this lost reflected radiation can be captured by the next collector assembly in the row representing an energy gain, called end gain, that partially offsets the end loss. The End Loss factor is calculated with equation 3.12 where L_f is the collector's focal length and $L_{f,eff}$ is the effective focal length. The effective focal length is calculated with equation 3.13 (WAGNER, GILMAN, 2011).

$$\eta_{EndLoss} = 1 - \frac{L_{f,eff} \tan(\theta)}{L_{sca}} + \frac{L_{f,eff} \tan(\theta) - L_{btw.sca}}{L_{sca}} \quad (3.12)$$

$$L_{f,eff} = \sqrt{\frac{\left(4L_f^2 + \left(\frac{L_{ap}}{2}\right)^2\right)^2}{L_f^2}} \cdot \frac{12L_f^2 + \frac{L_{ap}}{2^2}}{12(4L_f^2 + \frac{L_{ap}}{2^2})} \quad (3.13)$$

As it is calculated, different collectors have different end losses. The first collector in a row has no end gain. On an attempt of simplification, it will be assumed that the end loss is an average value of the end loss of the collectors in the loop (two with end gain and two without end gain).

3.5.4.4 Cleanliness factor

According to Paraschiv et al. (2010), the cleanliness factor for ET-150 parabolic collectors has a value of 0.97.

3.5.5 Solar field absorbed energy

The HCE's absorbed useful energy collected by an assembly can be defined as the difference between the radiant energy absorbed and heat lost by the HCE. This absorbed energy can be calculated by using equation 3.14, equation 3.15 and equation 3.16 where DNI_{av} is the available irradiance, \dot{q}'_{ABS} is absorbed energy linear flux in the HCE, \dot{q}'_{HL} is the energy loss linear flux in the HCE, \dot{q}_{USEFUL} is the absorbed useful energy rate, in other words, the rate at which energy is carried by the HTF, and L_{SCA} is the assembly length.

$$DNI_{av} = DNI \cdot \eta_{opt} \cdot \cos(\theta) \quad (3.14)$$

$$\dot{q}'_{ABS} = DNI_{av} \cdot L_{ap} \quad (3.15)$$

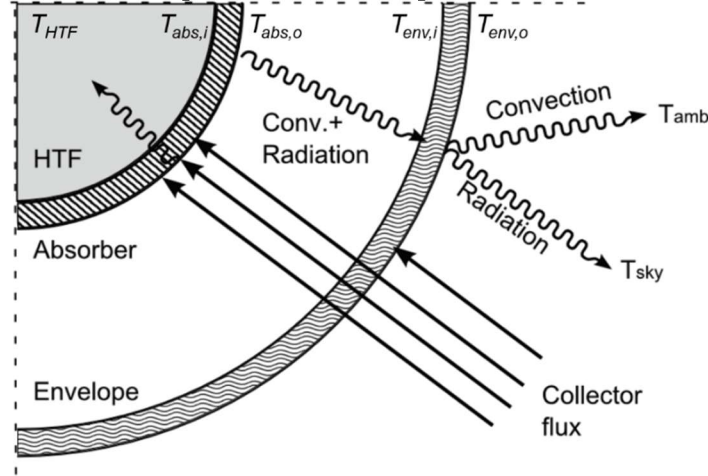
$$\dot{q}_{USEFUL} = (\dot{q}'_{abs} - \dot{q}'_{HL}) \cdot L_{SCA} \quad (3.16)$$

It is important to note that, as the temperature of the HTF changes through the different assemblies of the loop, the heat losses and the amount of energy absorbed by the HTF have different values for different assemblies in the loop.

The HCE heat loss for each collector is calculated in the via an iterative method based in the temperature in the absorber tube's outer surface and the glass envelope's inner surface as described by Wagner e Gilman (2011). The calculation of the heat loss can be divided in, first, setting a guess value for the temperatures across the HCE's cross-section based in the HTF temperature coming from the cold storage tank, determining the systems thermal resistances for those temperatures, calculating the heat loss. After the first iteration, the temperatures across the HCE cross-section are recalculated and used to determine the heat loss once again. This

procedure repeats itself until a stopping criterion is met. The heat transfer phenomena and temperature distribution across the HCE can be seen in the illustration of figure 16.

Figure 15 - Heat transfer phenomena and temperature distribution across the HCE



Source: Adapted from Wagner e Gilman (2011).

On a given timestep, the guess temperature distribution can be done with equation 3.17 to equation 3.20. In these equations, T_{HTF} is the HTF temperature, $T_{abs,i}$ is the temperature in the absorber inner surface, $T_{abs,o}$ is the temperature in the absorber outer surface, $T_{env,i}$ is the temperature in the glass envelope inner surface, $T_{env,o}$ is the temperature in the glass envelope outer surface, T_{amb} is the environment's dry bulb temperature. All temperatures used in the heat loss calculation are in Kelvin (K).

$$T_{abs,i} = T_{HTF} + 2 \quad (3.17)$$

$$T_{abs,o} = T_{abs,i} + 5 \quad (3.18)$$

$$T_{env,i} = T_{abs,o} - 0.8 \cdot (T_{abs,o} - T_{amb}) \quad (3.19)$$

$$T_{env,o} = T_{env,i} - 2 \quad (3.20)$$

The determination of the HCE's thermal resistances also follows an iterative process that solves the thermal problem for the heat transfers and interactions between the HCE and the ambient in a similar fashion to solving an electrical circuit. Each thermal interaction has its resistance that can be summed up to represent the whole thermal circuit.

Six different thermal interactions can be accounted in the HCE: the forced convection between HTF and absorber tube (HTF_{abs}), the conduction through the absorber tube (abs_{abs}), the radiation between absorber and glass envelope (abs_{env}), the conduction through the glass envelope (env_{env}), the connection between the glass envelope and environment (env_{amb}) and the radiation between the envelope and environment (env_{sky}). The convection inside the cavity

between absorber tube and glass envelope is not accounted by considering the existence of permanent vacuum in that region. The physical modeling of each resistance can be found in Appendix B.

With the resistances defined, it is possible to calculate the collector assembly linear heat loss, as seen in equation 3.21 where. Next, the temperature distribution is recalculated based in the heat loss just found, equation 3.22 to 3.25.

$$\dot{q}'_{HL} = \frac{R_{env_sky} \cdot (T_{abs,o} - T_{sky}) + R_{env_amb} \cdot (T_{abs,o} - T_{amb})}{R_{abs_env} \cdot R_{env_amb} + R_{env_env} \cdot R_{env_amb} + R_{abs_env} \cdot R_{env_sky} + R_{env_env} \cdot R_{env_sky} + R_{env_amb} \cdot R_{env_sky}} \quad (3.21)$$

$$T_{tb,i} = T_{htf} + (\dot{q}'_{abs} - \dot{q}'_{HL}) \cdot R_{HTF_abs} \quad (3.22)$$

$$T_{tb,o} = T_{tb,i} + (\dot{q}'_{abs} - \dot{q}'_{HL}) \cdot R_{abs_abs} \quad (3.23)$$

$$T_{env,i} = T_{tb,o} - \dot{q}'_{HL} \cdot R_{abs_env} \quad (3.24)$$

$$T_{env,o} = T_{env,i} - \dot{q}'_{HL} \cdot R_{env_env} \quad (3.25)$$

The iterative process stops when the stop criteria described by equation 3.26, gets smaller than 0.05 or the number of iterations is bigger than 4.

$$StopCrit_{HL} = \sqrt{\left(\frac{T_{tb,o,past} - T_{tb,o}}{T_{tb,o}}\right)^2 + \left(\frac{T_{env,i,past} - T_{env,i}}{T_{env,i}}\right)^2} \quad (3.26)$$

3.5.6 Nodal energy balance

It is necessary to solve the energy balance across the solar field loop for a given timestep to find the solar field outlet HTF temperature. The energy balance problem is solved in this work with the use of the nodal assembly approach proposed by Wagner e Gilman (2011). In this approach, the collector assembly's energy balance counts with transient terms and is made for each assembly.

The energy balance for the HCE control volume of a single SCA node take into consideration the HTF's inlet energy flow ($\dot{q}_{SCA,i}$), the outlet energy flow ($\dot{q}_{SCA,o}$), the absorbed energy (positive for net absorption and negative for net loss), and the internal energy term (U), equation 3.27. From this expression, the inlet and outlet energy flows can be rearranged and expressed as in equation 3.28, where m_{HTF} is the HTF's mass inside an assembly's HCE, \dot{m}_{HTF} is the mass flow rate passing through the assembly, and consequently through the loop, c_{HTF} is the HTF's specific heat calculated at nodal average temperature, $T_{HTF,SCA,i}$ and $T_{HTF,SCA,o}$ are

the assembly inlet and outlet HTF temperatures and $\bar{T}_{HTF,SCA}$ is the assembly's nodal average temperature. The internal energy can be expressed as in equation 3.29.

$$\dot{q}_{SCA,i} + \dot{q}_{USEFUL} = \frac{\partial U}{\partial t} + \dot{q}_{SCA,o} \quad (3.27)$$

$$\dot{q}_{SCA,i} - \dot{q}_{SCA,o} = \dot{m}_{HTF} \cdot c_{HTF} \cdot (T_{HTF,SCA,i} - T_{HTF,SCA,o}) = 2 \cdot \dot{m}_{HTF} \cdot c_{HTF} \cdot (T_{HTF,SCA,i} - \bar{T}_{HTF,SCA}) \quad (3.28)$$

$$\frac{\partial U}{\partial t} = m_{HTF} \cdot c_{HTF} \cdot \frac{\partial T}{\partial t} \quad (3.29)$$

With the substitution of the previous expression onto the energy balance equation, the equation ends as a linear differential equation, equation 3.30, with general solution expressed by equation 3.31 and equation 3.32 where Δt is the time step length. The assembly node outlet temperature can be found using the average temperature definition as in equation 3.33. The unknown constant $C1$ is found by enforcing the boundary condition that the average nodal temperature at the beginning of the time step is equal to the average nodal temperature at the end of the previous time step.

As the calculated temperature for each node depends on both the inlet temperature of the previous assembly and the average node temperature from the previous time step, these values must be established as boundary conditions. The temperature of the SCA node at the previous time step is stored every time step while the inlet temperature, for the assemblies after the first SCA, is set equal to the outlet temperature of the previous node as means of fulfilling this boundary conditions

$$\frac{\partial \bar{T}}{\partial t} = \frac{2 \cdot \dot{m}_{HTF} \cdot (T_{SCA,i} - \bar{T}_{SCA}) + \dot{q}_{USEFUL}}{m_{HTF} \cdot c_{HTF}} \quad (3.30)$$

$$\bar{T}_{SCA} = \frac{\dot{q}_{USEFUL}}{2 \cdot \dot{m}_{HTF} \cdot c_{HTF}} + C1 \cdot \exp \left[-\frac{2 \cdot \dot{m}_{HTF} \cdot c_{HTF}}{m_{HTF} \cdot c_{HTF}} \cdot \Delta t \right] \quad (3.31)$$

$$C1 = \bar{T}_{SCA,past} - \frac{\dot{q}_{USEFUL}}{2 \cdot \dot{m}_{HTF} \cdot c_{HTF}} - T_{SCA,i} \quad (3.32)$$

$$T_{SCA,o} = 2 \cdot \bar{T}_{SCA} - T_{SCA,i} \quad (3.33)$$

It is important to mention that this energy balance model does not account for the thermal inertia from the distribution piping and its transient effects. The HTF mass in the HCE is obtained by equation 3.34.

$$m_{HTF} = \rho_{HTF} \cdot L_{SCA} \cdot \pi \cdot \left(\frac{D_{abs,i}}{2} \right)^2 \quad (3.34)$$

3.5.7 Heat transfer fluid freezing protection

During the night or in periods of low radiation, if the temperature of the HTF at the end of a collector assembly falls under the minimum allowed temperature ($T_{HCE,FP}$) of 265 °C, the SCA outlet temperature is set to 265 °C and the freezing protection heat used to keep the HTF from solidifying can be calculated via equation 3.35.

$$\dot{q}_{HCE,FP} = \dot{m}_{HTF} \cdot c_{HTF} \cdot (T_{HCE,FP} - \bar{T}_{SCA}) \quad (3.35)$$

3.5.8 Mass flow rate controller

The mass flow controller is a logical controller implemented as an iterative process divided into two parts. The first part of the controller consists of determining the time step initial guess value for mass flow rate. After analyzing the available radiation data, a linear relationship between the guess mass flow rate and the available irradiance was drawn. For radiation values smaller than 100 W/m², the mass flow rate is set to the minimum limit while, for values above 100 W/m², the mass flow rate is given by equation 3.36.

$$\dot{m}_{HTF,guess} = 0.0068 \cdot DNI_{av} - 0.036 \quad (3.36)$$

With the loop absorbed useful heat, meaning the sum of the absorbed heat for each assembly in the loop, and with loop outlet temperature, which is the outlet temperature of the last SCA in the loop, obtained with the guessed mass flow rate, the mass flow rate value is recalculated and adjusted via equation 3.37. This new value is then reintroduced as the mass flow rate of the next iteration. The controller is set to adjust the mass flow so that the loop outlet temperature is maximized. Nonetheless, limitations are made so that the loop outlet temperature does not get higher than the solar field outlet nominal temperature of 550 °C.

The process described before repeats itself until the solar field outlet temperature is between 549.85 °C and 550 °C and the stop criterium, equation 3.38 and equation 3.39, fall under the threshold of 0.00001. Furthermore, if, in a given iteration, the new value of mass flow rate found is smaller than the minimum mass flow rate, the next iteration's mass flow rate is corrected to the minimum value. The same kind of correction happens if the newly calculated mass flow rate is above the maximum mass flow rate.

$$\dot{m}_{HTF} = \frac{\dot{q}_{USEFUL,loop}}{c_{HTH} (T_{SF,nom} - T_{SF,i})} \quad (3.37)$$

$$StopCrit_{controller} = \sqrt{\left(\frac{T_{SF,o} - T_{SF,o,past}}{T_{SF,o}}\right)^2 + \left(\frac{\dot{m}_{HTF} - \dot{m}_{HTF,past}}{\dot{m}_{HTF}}\right)^2} \quad (3.38)$$

$$StopCrit_{var} = abs(StopCrit_{controller} - StopCrit_{controller,past}) \quad (3.39)$$

The mass flow rate limits used by the controller are calculated using equation 3.40 and equation 3.41, respectively, where, $v_{HTF,min}$ is the minimum flow speed allowed in the solar field loop and $v_{HTF,max}$ is the maximum flow speed allowed in the solar field loop. In this work, the mass flow rate limits were determined based on the NREL software System Advisor Model (SAM) suggested solar salt minimum and maximum solar field flow velocity of 0.116 m/s and 1.437 m/s respectively. These velocity values result in a minimum loop mass flow rate of 0.71 kg/s and a maximum loop mass flow rate of 8.2 kg/s.

$$\dot{m}_{HTF,min} = v_{HTF,min} \cdot \rho_{HTF(T_{SF,o,nom})} \cdot \pi \cdot \left(\frac{D_{abs,i}}{2}\right)^2 \quad (3.40)$$

$$\dot{m}_{HTF,max} = v_{HTF,max} \cdot \rho_{HTF(T_{SF,i,nom})} \cdot \pi \cdot \left(\frac{D_{abs,i}}{2}\right)^2 \quad (3.41)$$

3.5.9 Collector defocusing

As in the performed simulations the mass flow rates obtained did not reach the maximum value at any time, the collector defocusing model to tackle HTF over-heating was not needed since there is no scenario in which the mass flow rate controller cannot maintain the HTF temperature at its operational limit.

3.5.10 Solar field nominal parameters

The solar field nominal parameters used in the plant simulation can be found at table 6.

Table 6 -Solar field nominal parameters

Parameter	Value	Unit
Nominal irradiance (DNI_{nom})	966.5	W/m ²
Nominal optical efficiency ($\eta_{opt,nom}$)	0.73	-
Solar Multiple (SM)	2	-
Number of assemblies per loop (N_{SCA})	4	-
Number of loops in the solar field (N_{loop})	80	-
Net solar field collection area	261600	m ²
Distance between assemblies in a row (L_{btw_sca})	11	m
Distance between rows (L_{btw_rows})	18	m
Nominal inlet temperature ($T_{SF,i,nom}$)	550	°C
Nominal outlet temperature ($T_{SF,o,nom}$)	280	°C
HTF minimum temperature ($T_{HTF,min}$)	260	°C
Loop minimum mass flow rate ($\dot{m}_{loop,min}$)	0.71	kg/s
Loop maximum mass flow rate ($\dot{m}_{loop,max}$)	8.04	kg/s

3.6 THERMAL ENERGY STORAGE

The thermal energy storage is the CSP plant system that is responsible for storing the energy harnessed from the sun in the solar field. As indicated in section 3.1, the storage system modeled is composed of two tanks, one containing hot fluid, at a nominal temperature of 550°C, and another containing cold fluid, at a nominal temperature of 280°C. In EES, the model developed solves the mass and energy balances for both the tanks in a simultaneous interactive process. For simplification, stored fluid stratification was not accounted, and therefore the model treats the fluid in tanks as a homogeneous.

3.6.1 Storage tank sizing

Defining the storage tank dimensions starts by establishing the TES thermal capacity (E_{TES}), equation 3.42. The thermal capacity amounts the thermal energy necessary to feed the power block on nominal conditions and full load production during a given number of hours. In equation 3.42, $P_{gross,nom}$ is power block's nominal gross power output and Δt_{TES} is the number of hours the TES can feed the power block at nominal conditions, also known as storage time.

$$E_{TES} = \frac{P_{gross,nom} \cdot \Delta t_{TES} \cdot 3600}{\eta_{PB}} \quad (3.42)$$

The salt mass necessary to store an amount of energy equivalent to the thermal capacity for the given hot and cold tanks nominal temperatures, $T_{HT,nom}$ and $T_{CT,nom}$ respectively, can be calculated by equation 3.43. Besides the thermal capacity, equation 3.41 takes in account actual TES tanks' constructive limitations. In real tanks, the salt pump headers can't reach the last 5% of the salts volume (BIENCINTO et al., 2014).

$$m_{TES} = 1.05 \left(\frac{E_{TES}}{c_{HTF} (T_{HT,nom} - T_{CT,nom})} \right) \quad (3.43)$$

The next step in the storage sizing is calculating the tanks' volume. The volume for each tank can be calculated with equation 3.44 where the specific mass (ρ_{HTF}) for each tank is calculated for their nominal temperature. An extrapolation of 10% is made on the volume of both tanks as this extra space is required as a security measure in real tanks (BIENCINTO et al., 2014) . When calculating *Tank* parameters, it is necessary to choose one of the tanks performing the calculation with the corresponding tank's properties and parameters.

$$V_{Tank} = 1.1 \left(\frac{m_{TES}}{\rho_{HTF}(T_{Tank,nom})} \right) \quad (3.44)$$

Afterward, with a fixed height (H_{TES}) of 14 m, it is possible to calculate each tank's diameter (D_{Tank}) with equation 3.45 and then the tank external surface area (A_{Tank}) with equation 3.46.

$$D_{Tank} = 2 \cdot \left(\frac{V_{Tank}}{\pi \cdot H_{TES}} \right) \quad (3.45)$$

$$A_{Tank} = \pi \cdot D_{Tank} \cdot H_{TES} + \frac{\pi \cdot D_{Tank}^2}{2} \quad (3.46)$$

For the TES sizing model described, the variable that can be chosen to determine the TES size is the storage time. The plant simulated in this work has a storage time of 15 hours. This storage time was chosen because it is between the 11.5 hours average night duration and performed in this work

3.6.2 Hot tank mass and energy balances

As a control volume, the hot tank counts with an inlet mass and energy flow from the solar field ($\dot{m}_{HT,i_{SF}}, \dot{q}_{HT,i_{SF}}$), an outlet mass and energy flow to the power block heat exchangers ($\dot{m}_{HT,o_{PB}}, \dot{q}_{HT,o_{PB}}$) and the stored fluid and its energy (m_{HT}, Q_{HT}). Based on this description, the mass balance for the hot tank can be represented by equation 3.47. In this equation, the known parameters at the beginning of the time step (t) are used to determine the salt mass in the tank at the end of the time step ($t + \Delta t$).

$$\dot{m}_{HT,i_{SF},t} - \dot{m}_{HT,o_{PB},t} = \frac{m_{HT,t+\Delta t} - m_{HT,t}}{\Delta t} \quad (3.47)$$

Next, the total energy balance for the same control volume is expressed by equation 3.48 where T_{ref} is the reference temperature, set at 25°C. This equation is used to determine the tank's fluid temperature at the end of the time step.

$$\dot{q}_{HT,i_{SF},t} - \dot{q}_{HT,o_{PB},t} - \dot{q}_{HT,HL} + \dot{q}_{HT,FP} = \frac{m_{HT,t+\Delta t} \cdot c_{(T_{HT,t+\Delta t})} \cdot (T_{HT,t+\Delta t} - T_{ref}) - Q_{HT,t}}{\Delta t} \quad (3.48)$$

$$\dot{q}_{HT,i_{SF},t} = \dot{m}_{HT,i_{SF},t} \cdot c_{(T_{HT,i_{SF},t})} \cdot (T_{HT,i_{SF},t} - T_{ref}) \quad (3.49)$$

$$\dot{q}_{HT,o_{PB},t} = \dot{m}_{HT,o_{PB},t} \cdot c_{(T_{HT,o_{PB},t})} \cdot (T_{HT,o_{PB},t} - T_{ref}) \quad (3.50)$$

$$Q_{HT,t} = m_{HT,t} \cdot c_{(T_{HT,t})} \cdot (T_{HT,t} - T_{ref}) \quad (3.51)$$

These two balances can then be solved by the introduction of a linearized relationship between the outlet mass flow rate at the beginning of the time step and the lastly found tank's fluid temperature at the end of the time step better explained in section 3.7.

3.6.3 Cold tank mass and energy balances

The mass balance over the cold tank control volume is expressed by equation 3.52. This control volume encompasses the inlet mass flow and energy flux coming from the heat exchangers of the power block ($\dot{m}_{CT,i_{PB}}, \dot{q}_{CT,i_{PB}}$), the inlet flow coming from the recirculation system ($\dot{m}_{CT,i_{recirc}}, \dot{q}_{CT,i_{recirc}}$), the outlet flow that goes to the solar field ($\dot{m}_{CT,o_{SF}}, \dot{q}_{CT,o_{SF}}$) and the stored fluid and its energy (m_{CT}, Q_{CT}). Similar to the mass balance in the hot tank, the mass balance in the cold tank is used to determine the mass contained in the tank by the end of the time step.

$$\dot{m}_{CT,i_{PB},t} + \dot{m}_{CT,i_{recirc},t} - \dot{m}_{CT,o_{SF},t} = \frac{m_{CT,t+\Delta t} - m_{CT,t}}{\Delta t} \quad (3.52)$$

The energy balance over the cold tank control volume is expressed by equation 3.53. Again, similarly to the hot tank, the cold tank energy balance is used to estimate the tank's fluid temperature at the end of the time step.

$$\dot{q}_{CT,i_{PB},t} + \dot{q}_{CT,i_{recirc},t} - \dot{q}_{CT,o_{SF},t} - \dot{q}_{CT,HL} + \dot{q}_{CT,FP} = \frac{m_{CT,t+\Delta t} \cdot c_{(T_{CT,t+\Delta t})} \cdot (T_{CT,t+\Delta t} - T_{ref}) - Q_{CT,t}}{\Delta t} \quad (3.53)$$

$$\dot{q}_{CT,i_{PB},t} = \dot{m}_{CT,i_{PB},t} \cdot c_{(T_{CT,i_{PB},t})} \cdot (T_{CT,i_{PB},t} - T_{ref}) \quad (3.54)$$

$$\dot{q}_{CT,i_{recirc},t} = \dot{m}_{CT,i_{recirc},t} \cdot c_{(T_{CT,i_{recirc},t})} \cdot (T_{CT,i_{recirc},t} - T_{ref}) \quad (3.55)$$

$$\dot{q}_{CT,o_{SF},t} = \dot{m}_{CT,o_{SF},t} \cdot c_{(T_{CT,o_{SF},t})} \cdot (T_{CT,o_{SF},t} - T_{ref}) \quad (3.56)$$

$$Q_{CT,t} = m_{CT,t} \cdot c_{(T_{CT,t})} \cdot (T_{CT,t} - T_{ref}) \quad (3.57)$$

To solve the cold tank's balances, the cold tank's inlet mass flow rate coming from the power block is set equal to the hot tank's outlet mass flow rate while the temperature of the incoming fluid from the power block is fixed in 278,7°C.

3.6.4 Tank heat loss

The model developed in EES accounts for heat loss in the tanks. The heat loss can be calculated for each tank by using equation 3.58 with their respective parameters. Equation 3.58 was derived from heat loss measurements done in the storage tanks from the Solar Two Solar Tower plant (HERRMANN, KELLY, PRICE, 2004).

$$\dot{q}_{Tank,HL} = 1000 \cdot (0.00017 \cdot T_{Tank,t} + 0.012) \cdot A_{Tank} \quad (3.58)$$

3.6.5 Tank temperature control

As in the solar field, the solidification or excessive temperature fall are points that must be controlled in the storage tanks. The control is made by a safety heating system. When the salt in the hot tank has its fluid temperature falling below its minimum level of 520°C, it gets heated. Likewise, when the salt stored in the cold tank has its temperature falls below the temperature of 265°C, heat is introduced to keep it above this level. Equation 3.59 calculates the heat supplied to the tanks. $T_{TES,min}$ is the minimum temperature level possible in each tank.

$$\dot{q}_{Tank,FP} = m_{Tank,t+\Delta t} \cdot c_{(T_{Tank,min})} \cdot (T_{Tank,min} - T_{Tank,t+\Delta t}) \quad (3.59)$$

3.6.6 Thermal energy storage nominal parameters

The major nominal parameters from the thermal energy storage system can be seen in table 7.

Table 7 - Thermal energy storage nominal parameters

Parameter	Value	Unit
Storage time (Δt_{TES})	15	h
Thermal Capacity (E_{TES})	1357.1	MWh
Storage mass (m_{TES})	12546	ton
Tank height (H_{TES})	14	m
TES tanks' diameter (D_{HT}/D_{CT})	26.86/25.62	m
TES tanks' surface area (A_{HT}/A_{CT})	2314.1/2158.1	m ²
TES nominal temperatures ($T_{HT,nom}/T_{CT,nom}$)	550/280	°C
TES minimum temperatures ($T_{HT,min}/T_{CT,min}$)	520/260	°C

3.7 POWER BLOCK

The power block is the plant section that converts the thermal energy delivered by the hot storage tank into electricity. The Rankine cycle that does this conversion was implemented in *MATLAB* using the water/steam thermodynamic library XSteam (HOLMGREN, 2007). This implementation was then condensed to an equation to be used together with the hot storage tank model in EES.

The relationship that represents the power block in the EES simulation is built from some different assumptions. The first and most important assumption about the operation of the power block accounts for the power block to be working steadily on nominal conditions for any time step in which the hot storage tank has enough thermal energy, or in other words enough stored salt mass, to feed the power block's energy demand during that time step. The referred operation condition means constant energy flux through the heat exchangers, constant power block efficiency and fixed electrical power output. Moreover, the model assumes that the heat exchangers have constant nominal overall heat exchange coefficients (UA) and that the temperature of the salt leaving the power block exchanges entering the cold tank is fixed in 278°C.

With previous assumptions, it is possible to calculate the mass flow rate at which the hot tank storage, at a certain temperature, must supply salt to the power block heat exchangers

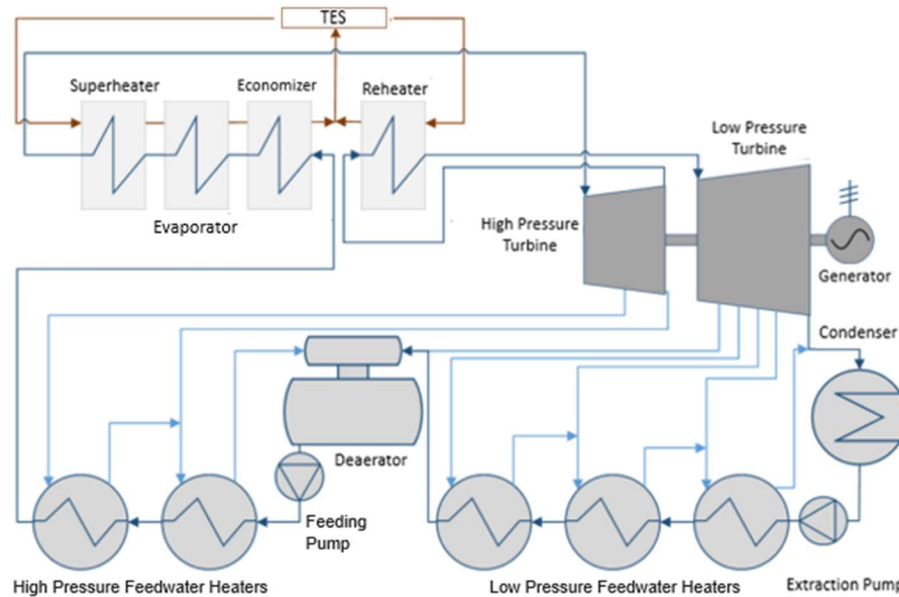
to match the energy flux demanded by the steam cycle at the nominal condition. Repeating this calculation for different storage fluid temperatures across the range of allowed temperatures in the hot tank (520°C-550°C) allows for the establishment of a linear relationship between the hot tank's temperature and the outlet temperature, equation 3.58. Equation 3.58 is a relationship with a 0.999 correlation coefficient.

$$\dot{m}_{HT,OPB,t} = (-0.921 \cdot T_{HT,t+\Delta t}) + 725.19 \quad (3.60)$$

3.7.2 The modeled Rankine cycle

The Rankine cycle modeled in this work is an adaptation of the simplified SEGS VI Rankine cycle suggested by Patnode (2006) and also applied by Sá (2013). Figure 16 shows an illustration of the original SEGS VI power block while figure 17 shows the adapted power block where feed-water heaters were substituted by open mixing vessels. In this simplified model, it is considered that the thermodynamic state of a power block component's outlet is kept as the thermodynamic state of the next component's inlet. Also, it is important to notice that this model does not consider pressure drops and water/vapor leakages. Each power block component model is described in Appendix C.

Figure 16 - SEGS VI power block layout



Source: Adapted from Sá (2013).

3.7.3 Plant net electrical power output definition

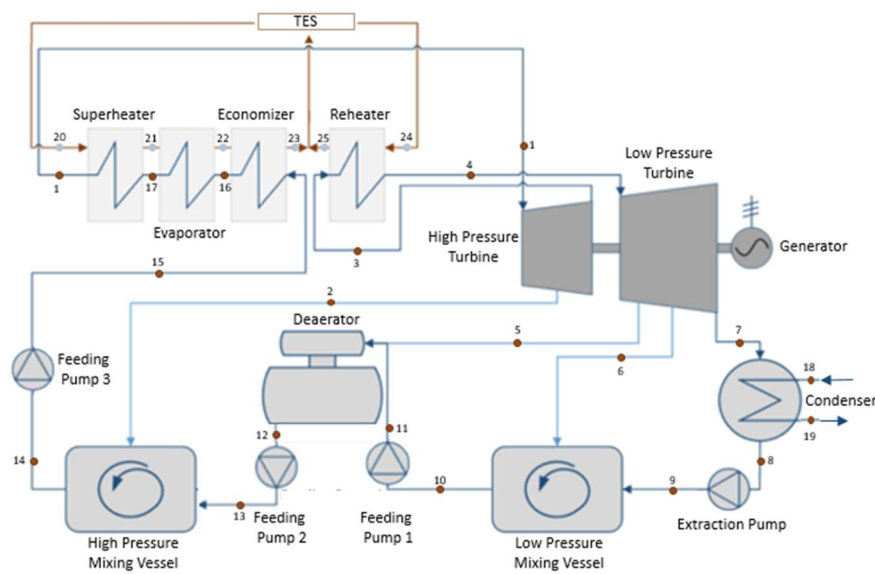
As seen in table 9, the nominal net electrical power output chosen for the plant was 30 MW_e . This choice was made based on a Brazilian federal law that gives electricity

distribution and electric grid usage taxes total waver to power station projects that use renewable energy sources such solar thermo power and inputs up until 30 MW_e in the national electric grid (ANEEL, 2007).

3.7.4 Power block nominal parameters

Figure 17 shows the modeled power block layout, and table 8 indicates the thermodynamic parameters for the different points in the Rankine cycle for nominal conditions. Table 9 indicates the general nominal power block parameters.

Figure 17 - Modeled Rankine cycle layout and thermodynamic cycle points



Source: Adapted from Sá (2013).

Table 8 - Rankine cycle thermodynamic parameters

Power Block Point Number	P [bar]	T [°C]	h [kJ/kg]	s [J/kg°C]	x [-]	\dot{m} [kg/s]
PB-1	100.00	540.00	3476.9	6.73	1	29.22
PB-2	50.00	436.50	3284.90	6.78	1	1.46
PB-3	15.00	286.17	3007.30	6.87	1	27.76
PB-4	15.00	393.66	3242.70	7.25	1	27.76
PB-5	8.50	321.58	3101.20	7.28	1	1.39
PB-6	2.50	190.23	2848.50	7.36	1	1.32
PB-7	0.10	45.81	2393.90	7.55	0.92	25.05
PB-8	0.10	45.81	191.81	0.65	0	25.05
PB-9	2.50	45.85	192.14	0.65	0	25.05
PB-10	2.50	77.58	324.95	1.05	0	26.37
PB-11	8.50	77.67	325.83	1.05	0	26.37
PB-12	8.50	110.65	464.60	1.43	0	27.76
PB-13	50	111.51	471.25	1.43	0	27.76
PB-14	50	144.63	611.93	1.78	0	29.22
PB-15	100.00	145.72	619.82	1.79	0	29.22
PB-16	100.00	310.99	1407.90	3.36	0	29.22
PB-17	100.00	310.99	2725.50	5.62	0	29.22
PB-18	-	25.00	104.83	-	0	1319.5
PB-19	-	35.00	146.84	-	0	1319.5
PB-20	-	550.00	-	-	0	204.17
PB-21	-	469.71	-	-	0	204.17
PB-22	-	345.08	-	-	0	204.17
PB-23	-	269.69	-	-	0	204.17
PB-24	-	550	-	-	0	22.60
PB-25	-	360	-	-	0	22.60

Table 9 - Power block nominal parameters

Parameter	Value	Unit
Net power output (P_{net})	30	MW
Gross power output (P_{gross})	35.29	MW
Power block Rankine cycle efficiency (η_{PB})	0.39	-
Gross to net power conversion efficiency ($\eta_{gross_to_net}$)	0.85	-
High-pressure turbine efficiency (η_{HPTurb})	0.85	-
Low-pressure turbine efficiency (η_{LPTurb})	0.88	-
Pump efficiency (η_{pump})	0.69	-
Overall Heat Transfer Coefficient Superheater (UA_{sup})	124.18	[kW/°C]
Overall Heat Transfer Coefficient Evaporator (UA_{eva})	475.20	[kW/°C]
Overall Heat Transfer Coefficient Economizer (UA_{eco})	330.70	[kW/°C]
Overall Heat Transfer Coefficient Reheater (UA_{reh})	59.40	[kW/°C]
Overall Heat Transfer Coefficient Condenser (UA_{cond})	3613.70	[kW/°C]

3.8 SIMULATION INITIAL CONDITIONS

Melting the salt inventory and getting it ready to be used in the solar field is a costly process, the initial mass and temperature in the tanks were chosen and calculated to minimize these costs. The hot tank starts the simulation with its 5% minimum volume, at the temperature of 540 °C, and the cold tank starts the simulation with the rest of the TES mass stored at the temperature of 280°C which means that at the first time step the solar field is fed with molten salt at 280°C.

3.9 OPERATION MODEL

The plant operation regards the interaction of the solar field with the storage tanks and the interaction of the storage tanks with the power block. First, due to the use of molten salt and its high freezing temperature, the solar field always has fluid passing through it. The HTF temperature is always kept between 260 °C and 550°C employing mass flow rate control and impedance heating. After passing through the solar field, the outlet salt flow can be directed to the hot tank or cold tank depending on the outlet temperature and the storage tanks' levels. At day, if the solar field outlet temperature is above 520°C, the molten salt flux is allowed to go to the hot tank. Below this temperature level, the fluid is recirculated to the cold tank which means that at night, when there is no insolation, the fluid is also directed back to the cold tank.

Recirculation of the solar field outlet can also happen depending on the storage tanks' volume levels. If the estimated hot storage tank volume on a given time step is above the hot tank's maximum volume, the solar field outlet is recirculated on that time step. Similarly, if the estimated volume for the cold tank on a given time step falls below the tank's minimum volume, the solar field outlet is also recirculated.

As the last two cases of HTF recirculation happen in periods of high insolation, the fluid recirculated would theoretically return to the cold tank at temperatures close or equal to 550°C. However, as during both of this recirculation cases, the cold tank is storing a small amount of salt, adding the high-temperature HTF coming from the solar field to the cold tank makes the tank's temperature to rise to a value close to the solar field's nominal temperature. Consequently, the rise of temperature in the cold tank allows for the molten salt to enter the solar field in the next time step at temperatures close to the solar field temperature limit.

This cold tank temperature rise generates inconsistencies in the calculation of the HCE thermal resistances since viscosity values calculated get too low resulting in complex number results and the simulation the simulation to crash. To avoid these inconsistencies, if the HTF is recirculated because of the conditions of storage limit conditions, the fluid is set to return to the

cold tank at a maximum temperature of 300°C. The temperature reduction is achievable in a real plant using defocusing the collectors in the solar field.

As explained before, as long as there is enough mass in the hot storage tank to feed the power block and match its thermal energy demand, the power block produces the net power output for the duration of the time step. No schedule is made for energy generation. However, at the beginning of the simulation, the power block only starts to work after the hot storage tank reaches 10% of its volume. Furthermore, the power block is also turned off when the estimated cold tank volume is above the cold tank's maximum.

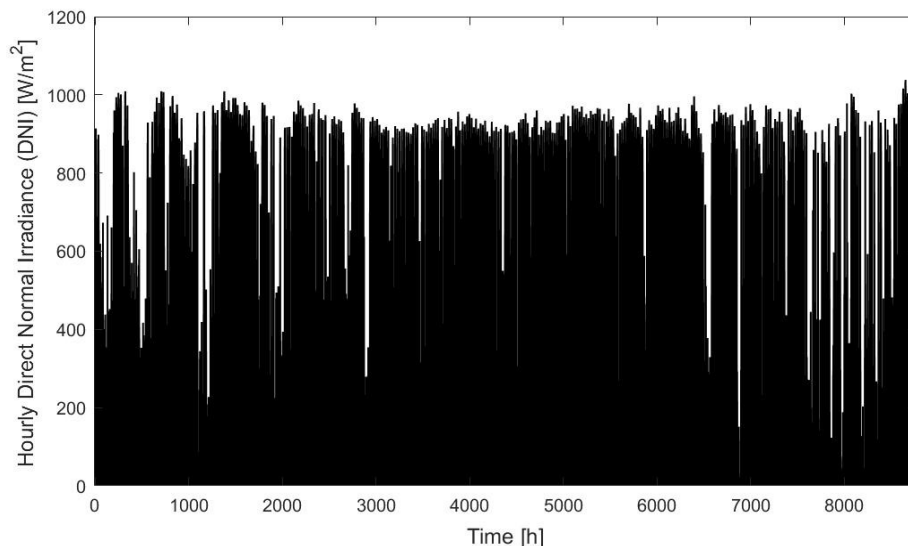
4 RESULTS AND DISCUSSION

This chapter deals with the results of the simulation performed using the models and descriptions made in the previous chapter. The modeled plant was simulated for a size defined by the solar multiple and the TES capacity, with values of 2 and 15h respectively. The main results presented in this section concern the plant's annual performance and the model validity verification.

3.10 ANNUAL PERFORMANCE

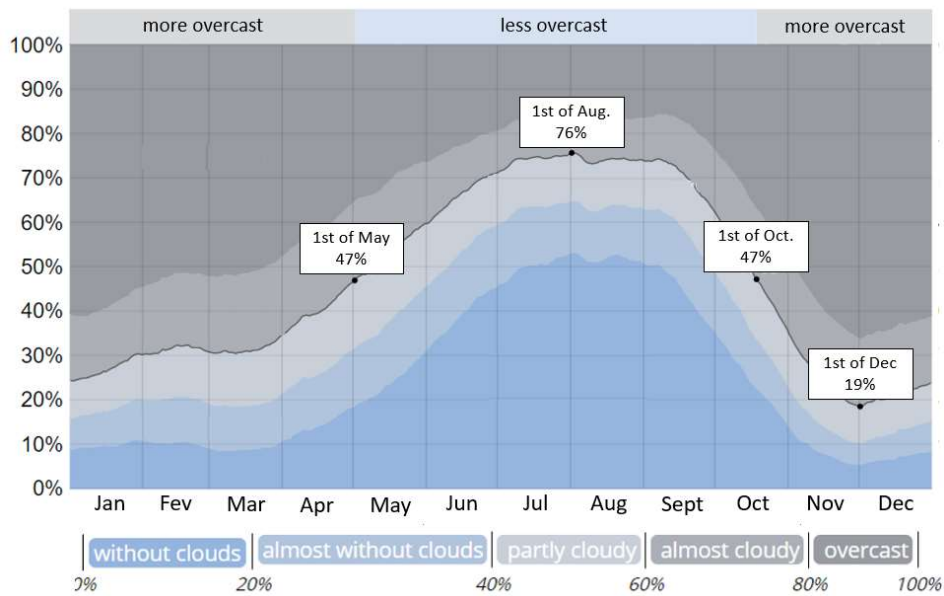
The generation of thermal energy, and consequently the generation of electrical energy, from a concentrated solar power plant, depends primarily on the available solar resources. Figure 18 shows the distribution of solar irradiation of a typical meteorological year. In this distribution, it is possible to observe that, for the period from October to April, the direct radiation incident on BJJ presents great variability unlike the period from April to September in which the incident radiation remains stable. This phenomenon is since in BJJ, as in much of northeastern Brazil, the year can be divided between the wet season and the dry season. While the beginning and end of the year is the rainy season, in which there is a significant presence of cloud cover, the middle of the year is the dry season presents clear skies, as can be seen in Figure 19.

Figure 18 - Annual distribution of hourly DNI



Source: Own authorship

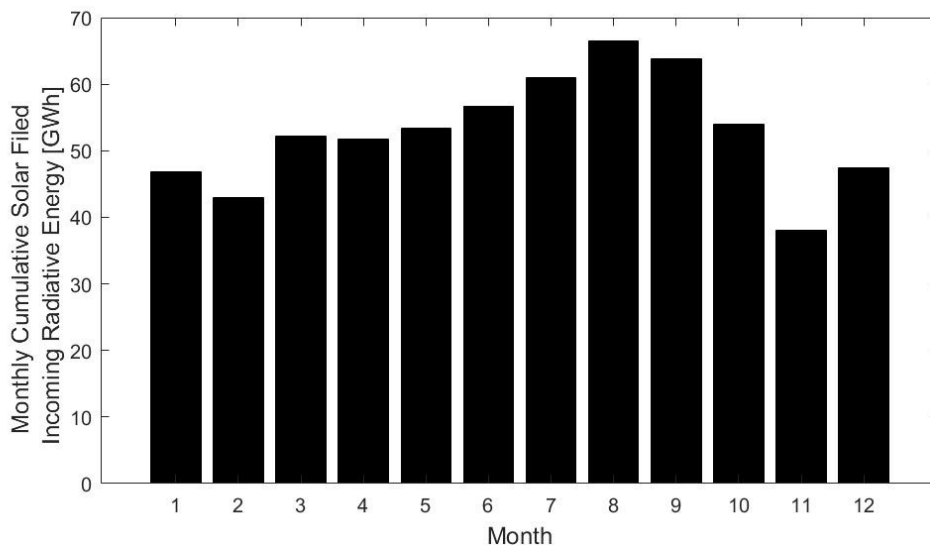
Figure 19 – Annual distribution of cloudiness in BJJ



Source: Weather Spark.

To better visualize the distribution of the radiation incident in BJJ as well as to facilitate future comparisons, figure 20 shows the annual distribution of accumulated radiative incident energy. In this figure, it is easy to notice that the months of the rainy season, October to March, have lower radiation than the months of the dry season, from April to September. It is also noted in figure 20 that the profile formed by the top of its bars presents similarity to the profile formed by the 'without clouds' region in figure 19.

Figure 20 – Annual distribution of monthly cumulative solar field incoming radiant energy

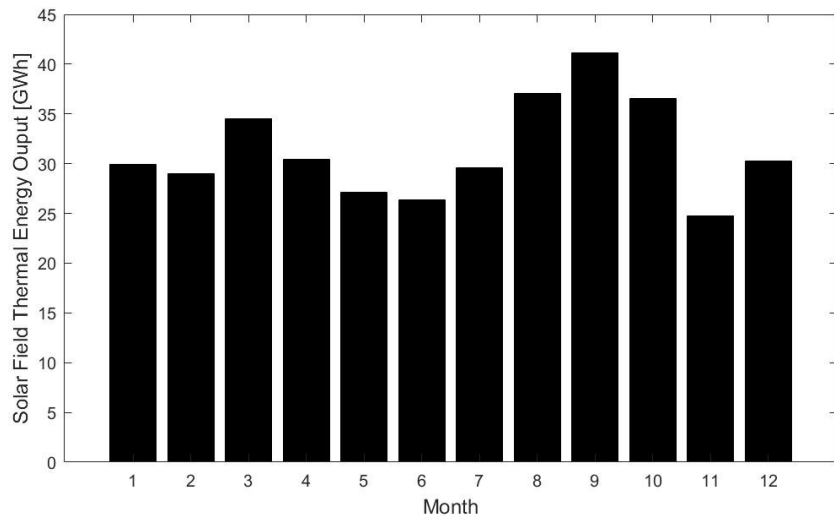


Source: Own authorship.

In figure 21 it is possible to visualize the accumulated monthly production of the useful thermal energy of the solar field. It is observed that unlike the available radiative energy, the thermal energy produced by the solar field has a decrease in April to July. This drop is caused by the combination of decreasing temperatures in the locality, figure 22, which increases the thermal losses as well as the decrease of the optical efficiency as a function of the variation of the declination and other solar angles. The monthly variation of the mean thermal efficiency of the solar field can be seen in figure 23.

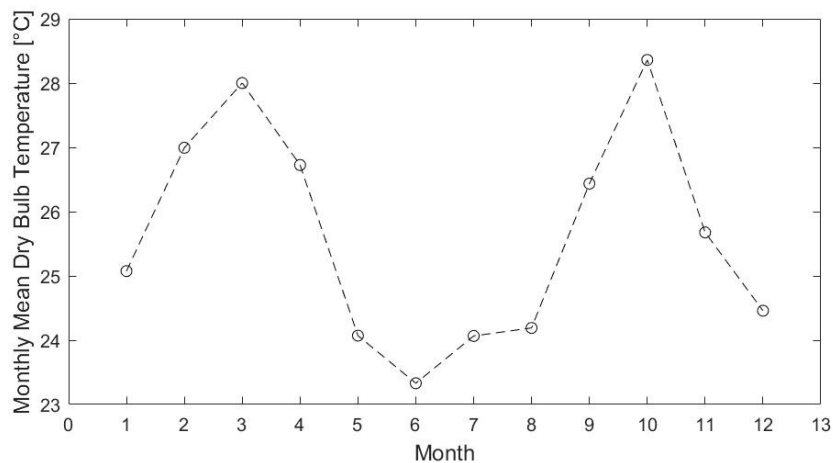
It is relevant to notice that the system's thermal energy has this profile throughout the year because no auxiliary heating system was used. In the case of one of these systems were used, the thermal input would be more evenly distributed throughout the year.

Figure 21 - Annual distribution of monthly cumulative solar field thermal energy output



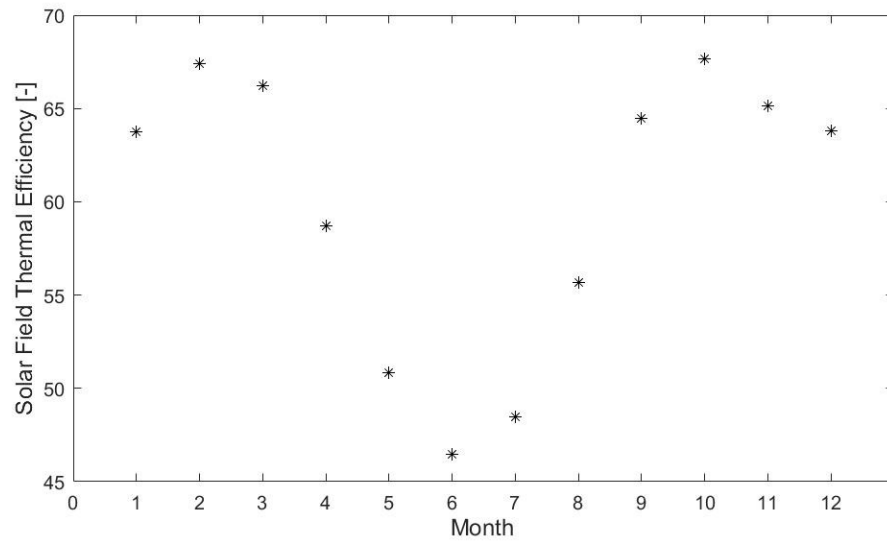
Source: Own authorship

Figure 22 - Annual distribution of monthly average dry bulb ambient temperature



Source: Own authorship.

Figure 23 - Annual distribution of monthly average solar field thermal efficiency



Source: Own authorship.

The amounts of the monthly distribution of generated electricity, the capacity factor, and solar-electric efficiency can be seen in Table 10.

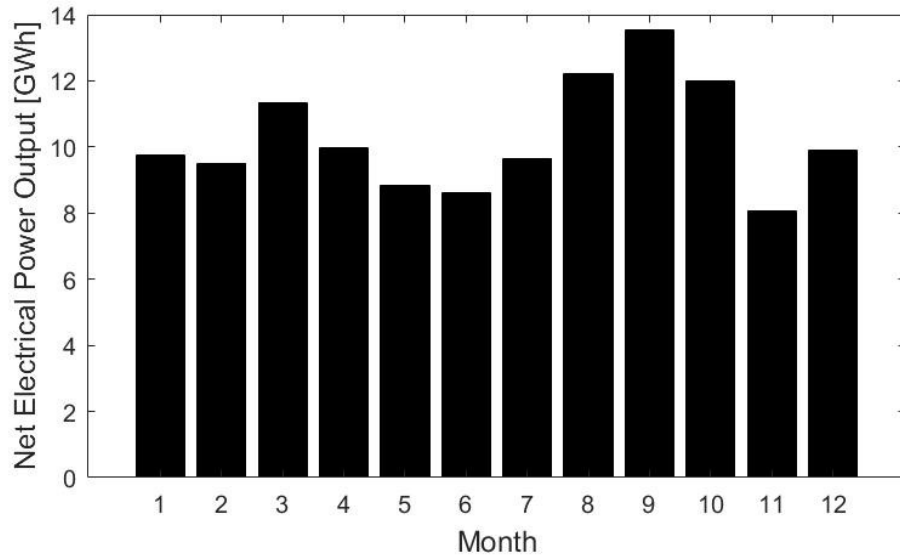
Table 10 - Main plant electric generation parameters

Month	Net Electrical Power Output [GWh]	Capacity Factor [-]	Solar-to-Electric Efficiency [-]
January	9.75	0.44	20.79
February	9.51	0.47	22.13
March	11.34	0.51	21.73
April	9.96	0.46	19.23
May	8.85	0.39	16.85
June	8.61	0.39	15.18
July	9.66	0.43	15.84
August	12.21	0.54	18.35
September	13.53	0.63	21.20
October	12.00	0.54	22.24
November	8.07	0.37	21.21
December	9.90	0.44	20.87

In the graphical distribution of the above results, Figure 24 to 26 shows that while the month of greatest electric generation in September, given the higher incidence of solar radiation, the highest solar-electric efficiency occurs in October, with a value of 22 %, as this month combines high ambient temperatures and intense incident solar radiation. It is also possible to verify that the lowest electric generation occurs in November, when there is the highest

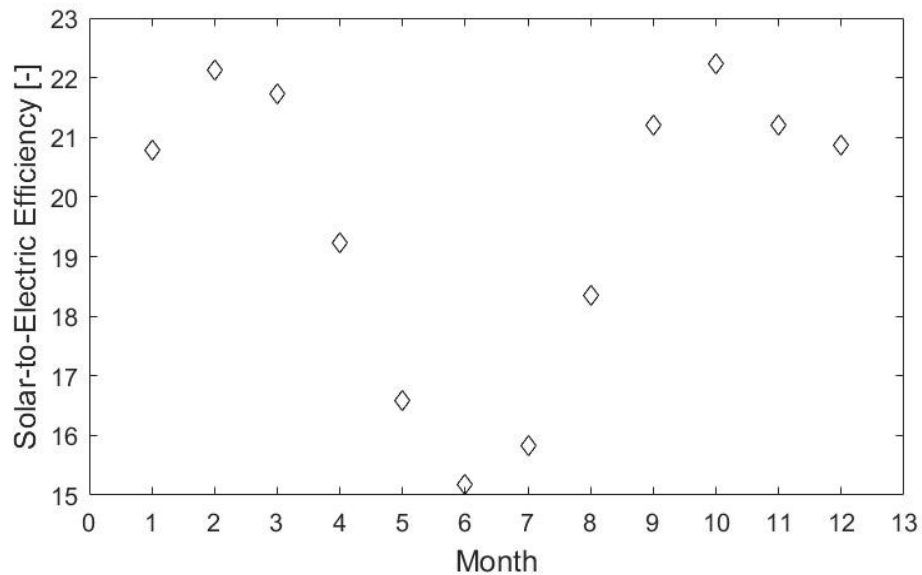
cloudiness rate of the year, as can be seen in figure 19. However, the lowest efficiency occurs in June, the month in which winter begins and thus the time of the lowest optical efficiency of the solar collectors.

Figure 24 - Annual distribution of monthly cumulative net electrical power output



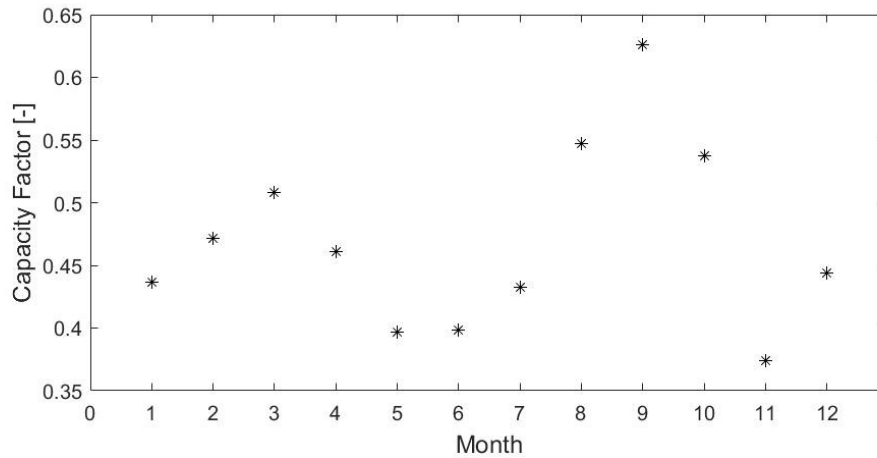
Source: Own authorship

Figure 25 - Annual distribution of monthly average solar-to-electric efficiency



Source: Own authorship

Figure 26 - Annual distribution of the capacity factor



Source: Own authorship.

Table 11 gives a summary of the main cumulative or average parameters of the plant for the total period of 1 year.

Table 11 - Main Annual performance parameters

Parameter	Value	Unit
Cumulative incoming radiant energy	634.78	[GWh]
Solar field thermal power output	376.63	[GWh]
Solar field thermal efficiency	0.593	[-]
Electric energy output	123.39	[GWh]
Capacity factor	0.469	[-]
Solar to electric efficiency	0.194	[-]

3.11 MODEL VALIDITY CHECK

To verify the validity of the model to represent the real system, a comparative analysis was performed between the results generated by the simulation of the plant in MATLAB and EES and the simulation made in SAM, a free software developed by NREL to analyze the operational and financial performance of various renewable sources, with equivalent parameters. It was decided to assess the validity of the model in this way because no experimental data on the operation of a parabolic trough plant with molten salt as heat transfer fluid was found.

In the modeling made in SAM, the physical characteristics of the modeled plant were implemented as well as the operating conditions and simplifying considerations were adapted

by adjusting the variables within the NREL software. The parameters used in the System Adviser Model are listed in table 12.

SAM has libraries for SCAs, HCEs and power blocks in which each listed component has its own optical and thermal efficiency models. Thus, in the verification simulation, it was decided to use the Eurotrough ET150 collector assembly and the heat collector element 2008 PTR70 with vacuum, throughout the solar field. The parameter values suggested by the software were maintained for each of them. Also, the choice of the 2008 PTR70 was because the HMS11 receiver was not listed in SAM and the chosen HCE was a similar option. As for the power block, the SEGS 30MWe Turbine model was chosen, and the efficiency of the thermodynamic cycle was altered to correspond to the Rankine cycle developed in this work.

Table 12 – SAM’s model parameters

Parameter	Value	Unit
Solar field		
HTF type	Hitec Solar Salt	
Solar Multiple	2	[-]
Distance between SCAs in a row	11	[m]
Distance between rows	18	[m]
Number of SCAs per row	4	[-]
Solar field nominal inlet temperature	280	[°C]
Solar field nominal outlet temperature	550	[°C]
Solar field initial temperature	280	[°C]
Piping heat loss at design temperature	0	[W/m ²]
Minimum HTF temperature	260	[°C]
Solar Multiple reference DNI	966.500	[W/m ²]
Optical efficiency	0.767	[-]
Collectors (SCAs) – Euro Trough ET150 (SAM’s library values)		
SCA length	150	[m]
SCA aperture	5.750	[m]
SCA aperture reflective area	817.500	[m ²]
Average focal length	2.100	[m ²]
Mirror reflectance	0.935	[-]
Receiver (HCEs) – 2008 Schott PTR70 Vacuum (SAM’s library values)		
Bellows shadowing	0.963	[-]
Envelope transmissivity	0.963	[-]
Envelope absorption	0.96	[-]
Power Block – SEGS 30 MWe Turbine		
Rated cycle conversion efficiency	0.392	[-]
Max turbine over design operation	1	[-]
Minimum turbine operation	0.2	[-]
Estimated gross to net conversion efficiency	0.85	[-]
Estimated Net output	30	[MW]
Fraction of thermal power for startup	0	[-]

Thermal Storage		
Equivalent full load hours of TES	15	h
Storage system configuration	Two Tank	[-]
Storage fluid type	Hitec Solar Salt	[-]
Turbine TES Adjustment – Efficiency	1	[-]
Turbine TES Adjustment – Gross Output	1	[-]
Tank heat losses	0.4	[MWh]
Parasitic		
Total design point parasitic	1.31	[MWe]

The comparative table 13 shows the main results of both simulated models. The results present a 1.54% difference to the MATLAB / EES model. This difference is caused by the fact that the SAM model represents the parasitic losses in a more detailed way considering losses for example with the cooling tower and the heat exchangers. The small difference indicates that the model developed in this work has good validity.

Table 13 - Model results comparative table

Parameter	MATLAB/EES	SAM
Net Electrical Power Output [GWh]	123.39	121.49
Capacity factor [-]	0.4695	0.4623

5 CONCLUSION

The present work proposed the analysis of the annual power generation performance of a concentrated solar power plant that uses parabolic trough technology and molten salt as heat transfer fluid. To do so, first, a background review on the subject was done from which knowledge was drawn to build a performance model for many of the plant's components. Next, an operation model was devised to allow for the simulation of the plant. Finally, the plant was simulated for the size defined by a solar multiple of 2 and a storage capacity of 15 hours.

The results of the simulation allowed the analysis of the electric power generation of the modeled plant during the typical year in Bom Jesus da Lapa (BA). From the figures obtained it is possible to identify the strong relationship between the electric power generation levels and the rain regime of the region. In the rainy season, from October to March, when there is much cloudiness, the availability of radiant energy is lower and therefore the generation is also reduced. In the dry season, from April to September, the climatic conditions are more stable.

However, despite the meteorological stability, in the period from April to July, the electricity production has a decrease given the decrease of the ambient temperature, which increases the thermal losses in the system, and the decrease of the optical efficiency of the collectors. Such a decrease in production shows the importance of the use of auxiliary systems of heating by hybridization of fuels that stabilize the supply of energy to the system.

Lastly, the plants model was verified using comparison with the results of a simulation in the software SAM. This comparison showed that the model developed represents reasonably the physical system. Therefore, based on the body of results obtained, it is concluded that the present work reaches the proposed objectives and brings contributions to the advancement of solar thermal energy in Brazil.

6 FUTURE WORK SUGGESTION

The topics presented below are suggestions for studies that can deepen the knowledge developed in this work:

- To model HTF distribution pipelines in the solar field and to analyze the influence of their inertia and thermal losses on the overall performance of the system;
- To analyze the introduction of auxiliary heating systems by fuel hybridization and its influence on the electricity generation;
- Model the power block for operation in partial loads and verify the impact of this configuration on the operation of the plant;
- Optimize solar field and thermal storage dimensions based on economic analysis to minimize LCOE;

REFERENCES

AK STEEL. 321 Stainless Steel: Data Sheet, 2012.

ANEEL – AGÊNCIA NACIONAL DE ENERGIA ELÉTRICA. **Resolução Normativa Nº 271**, 2007. 2 p. Disponível em: <<http://www2.aneel.gov.br/cedoc/ren2007271.pdf>>.

ANP – AGÊNCIA NACIONAL DO PETRÓLEO, GÁS NATURAL E BIOCMBUSTÍVEIS. Gasodutos de transporte - Movimentação, estocagem e comercialização de gás natural. Disponível em: <<http://www.anp.gov.br/movimentacao-estocagem-e-comercializacao-de-gas-natural/transporte-de-gas-natural/gasodutos-de-transporte>>. Acesso em: 31 dez. 2018.

ARCHIMEDE SOLAR ENERGY. **Concentrated Solar Power (CSP): The New Frontier of Molten Salts**, 2016.

BARLEV, David; VIDU, Ruxandra; STROEVE, Pieter. Innovation in concentrated solar power. **Solar Energy Materials and Solar Cells**, v. 95, n. 10, p. 2703–2725, 2011. BERGMAN, Theodore L.; LAVINE, Adrienne S.; INCROPERA, Frank P. **Fundamentals of Heat and Mass Transfer**. 7. ed. Somerset: Wiley, 2011.

BESARATI, S. M.; GOSWAMI, D. Y. Supercritical CO₂ and other advanced power cycles for concentrating solar thermal (CST) systems. In: BLANCO, M. J.; SANTIGOSA, L. R. (Org.). **Advances in Concentrating Solar Thermal Research and Technology**, Amsterdam: Elsevier, 2017.

BIENCINTO, Mario; GONZÁLEZ, Lourdes; ZARZA, Eduardo; DÍEZ, Luis E.; MUÑOZ-ANTÓN, Javier. Performance model and annual yield comparison of parabolic-trough solar thermal power plants with either nitrogen or synthetic oil as heat transfer fluid. **Energy Conversion and Management**, v. 87, p. 238–249, 2014.

BLANCO, M. J.; MILLER, S. Chapter 1: Introduction to concentrating solar thermal (CST) technologies. In: BLANCO, M. J.; SANTIGOSA, L. R. (Org.). **Advances in Concentrating Solar Thermal Research and Technology**, Amsterdam: Elsevier, 2017.

BURIN, Eduardo. **PLANTAS DE COGERAÇÃO DO SETOR SUCROALCOOLEIRO ASSISTIDAS POR CONCENTRADORES PARABÓLICOS**, 2015.

CASTAÑEDA, N.; VAZQUEZ, J.; DOMINGO, M. **Sener Parabolic trough Collector Design and Testing**. Seville, Spain, 2006. (13th SolarPACES Conference).

DESIDERI, U.; ZEPPARELLI, F.; MORETTINI, V.; GARRONI, E. Comparative analysis of concentrating solar power and photovoltaic technologies: Technical and environmental evaluations. **Applied Energy**, v. 102, p. 765–784, 2013.

DOMINGUEZ, R.; BARINGO, L.; CONEJO, A. J. Optimal offering strategy for a concentrating solar power plant. **Applied Energy**, v. 98, p. 316–325, 2012.

DUFFIE, John A.; BECKMAN, William A. **Solar engineering of thermal processes**. 3. ed. Hoboken, N.J.: Wiley, 2006.

ECK, M.; HIRSCH, T.; FELDHOFF, J. F.; KRETSCHMANN, D.; DERSCH, J.; MORALES, A. Gavilan; GONZALEZ-MARTINEZ, L.; BACHELIER, C.; PLATZER, W.; RIFFELMANN, K.-J.; WAGNER, M. Guidelines for CSP Yield Analysis – Optical Losses of Line Focusing Systems; Definitions, Sensitivity Analysis and Modeling Approaches. **Energy Procedia**, v. 49, p. 1318–1327, 2014.

EPE – EMPRESA DE PESQUISA ENERGÉTICA. **Balanco Energético Nacional 2018: Ano base 2017**. Rio de Janeiro.

FERNÁNDEZ-GARCÍA, A.; ZARZA, E.; VALENZUELA, L.; PÉREZ, M. Parabolic-trough solar collectors and their applications. **Renewable and Sustainable Energy Reviews**, v. 14, n. 7, p. 1695–1721, 2010.

FERRI, Roberta; CAMMI, Antonio; MAZZEI, Domenico. Molten salt mixture properties in RELAP5 code for thermodynamic solar applications. **International Journal of Thermal Sciences**, v. 47, n. 12, p. 1676–1687, 2008.

FORRISTALL, R. **Heat Transfer Analysis and Modeling of a Parabolic Trough Solar Receiver Implemented in Engineering Equation Solver**, 2003.

GEYER, Michael; LÜPFERT, Eckhard; OSUNA, Rafael; ESTEBAN, Antonio; SCHIEL, Wolfgang; SCHWEITZER, Axel; ZARZA, Eduardo; NAVA, Paul; LANGENKAMP, Josef; MANDELBERG, Eli. **Eurotrough - Parabolic Trough Collector Developed for Cost Efficient Solar Power Generation**. Zürich, Switzerland: Elsevier, 2002. (11th SolarPACES Conference).

GIL, Antoni; MEDRANO, Marc; MARTORELL, Ingrid; LÁZARO, Ana; DOLADO, Pablo; ZALBA, Belén; CABEZA, Luisa F. State of the art on high temperature thermal energy storage for power generation. Part 1—Concepts, materials and modellization. **Renewable and Sustainable Energy Reviews**, v. 14, n. 1, p. 31–55, 2010.

GREEN – GRUPO DE PESQUISA EM RECICLAGEM, EFICIÊNCIA ENERGÉTICA E SIMULAÇÃO NUMÉRICA. Smile Prroject. Disponível em: <<http://www.usp.br/green/smile.html>>. Acesso em: 19 jan. 2019.

GREEN, Martin A. Photovoltaic principles. **Physica E: Low-dimensional Systems and Nanostructures**, v. 14, n. 1, p. 11–17, 2002.

GUILLOT, Stéphanie; FAIK, Abdessamad; RAKHMATULLIN, Aydar; LAMBERT, Julien; VERON, Emmanuel; ECHEGUT, Patrick; BESSADA, Catherine; CALVET, Nicolas; PY, Xavier. Corrosion effects between molten salts and thermal storage material for concentrated solar power plants. **Applied Energy**, v. 94, p. 174–181, 2012.

GUIMARÃES, Ana Paula Cardoso; VIEIRA, Leonardo dos Santos Reis; SERRA, Eduardo Torres; MELO, SÉRGIO ROBERTO F.C. DE; MACEDO, NEY GUILHERME LEAL DE. **Caracterização de Localidades do Semi-Árido para Implementação de Um sistema Piloto Heliotérmico de Geração Elétrica**, 2010. 13 p. Acesso em: 4 jan. 2019.

GÜNTHER, Matthias; JOEMANN, Michael; CSAMBOR, Simon. Chapter 5: Parabolic Trough Technology. In: FEND, T.; QOAIDER, L. (Org.). **Advanced CSP Teaching Materials**: Deutsches Zentrums für Luft- und Raumfahrt e.V.; Institut für Elektrische Energietechnik - Universität Kassel, 2011, p. 106.

HERRMANN, Ulf; KEARNEY, David W. Survey of Thermal Energy Storage for Parabolic Trough Power Plants. **Journal of Solar Energy Engineering**, v. 124, n. 2, p. 145, 2002.

HERRMANN, Ulf; KELLY, Bruce; PRICE, Henry. Two-tank molten salt storage for parabolic trough solar power plants. **Energy**, v. 29, 5-6, p. 883–893, 2004.

HOLMGREN, Magnus. XSteam: Water and steam properties according to IAPWS IF-97. Disponível em: <<https://www.mathworks.com/matlabcentral/fileexchange/9817-x-steam-thermodynamic-properties-of-water-and-steam>>. Acesso em: 11 jan. 2019.

HOOMAN, K.; GUAN, Z.; GURGENCI, H. Advances in dry cooling for concentrating solar thermal (CST) power plants. In: BLANCO, M. J.; SANTIGOSA, L. R. (Org.). **Advances in Concentrating Solar Thermal Research and Technology**, Amsterdam: Elsevier, 2017.

IEA – INTERNATIONAL ENERGY AGENCY. **Technology Roadmap - Solar Thermal Electricity 2014**, 2014.

KEARNEY, D.; HERRMANN, U.; NAVA, P.; KELLY, B.; MAHONEY, R.; PACHECO, J.; CABLE, R.; POTROVITZA, N.; BLAKE, D.; PRICE, H. Assessment of a Molten Salt Heat Transfer Fluid in a Parabolic Trough Solar Field. **Journal of Solar Energy Engineering**, v. 125, n. 2, p. 170, 2003.

KEARNEY, D.; KELLY, B.; HERRMANN, U.; CABLE, R.; PACHECO, J.; MAHONEY, R.; PRICE, H.; BLAKE, D.; NAVA, P.; POTROVITZA, N. Engineering aspects of a molten salt heat transfer fluid in a trough solar field. **Energy**, v. 29, n. 5, p. 861–870, 2004.

KOLB, Gregory J.; HO, Clifford K.; MANCINI, Thomas R.; GARY, Jesse A. **Power Tower Technology Roadmap and Cost Reduction Plan**, 2011.

LÜPFERT, Eckhard; ZARZA-MOYA, Eduardo; GEYER, Michael; NAVA, Paul; LANGENKAMP, Josef; SCHIEL, Wolfgang; ESTEBAN, Antonio; OSUNA, Rafael; MANDELBERG, Eli. **Euro Trough Collector Qualification Complete - Performance Test Results from PSA**, 2003.

MACCARI, A.; BISSI, D.; CASUBOLO, G.; GUERRINI, F.; LUCATELLO, L.; LUNA, G.; RIVABEN, A.; SAVOLDI, E.; TAMANO, S.; ZUANELLA, M. Archimede Solar Energy Molten Salt Parabolic Trough Demo Plant: A Step Ahead towards the New Frontiers of CSP. **Energy Procedia**, v. 69, p. 1643–1651, 2015.

MADAENI, Seyed Hossein; SIOSHANSI, Ramteen; DENHOLM, Paul. **Capacity Value of Concentrating Solar Power Plants**, 2011. 49 p.

MALAGUETA, Diego; SZKLO, Alexandre; BORBA, Bruno Soares Moreira Cesar; SORIA, Rafael; ARAGÃO, Raymundo; SCHAEFFER, Roberto; DUTRA, Ricardo. Assessing incentive policies for integrating centralized solar power generation in the Brazilian electric power system. **Energy Policy**, v. 59, p. 198–212, 2013.

MONTES, M. J.; ABÁNADES, A.; MARTÍNEZ-VAL, J. M.; VALDÉS, M. Solar multiple optimization for a solar-only thermal power plant, using oil as heat transfer fluid in the parabolic trough collectors. **Solar Energy**, v. 83, n. 12, p. 2165–2176, 2009.

MORALES, A.; SAN VICENTE, G. Chapter 7: A new generation of absorber tubes for concentrating solar thermal (CST) systems. In: BLANCO, M. J.; SANTIGOSA, L. R. (Org.). **Advances in Concentrating Solar Thermal Research and Technology**, Amsterdam: Elsevier, 2017.

MOYA, E. Zarza. Chapter 5: Innovative working fluids for parabolic trough collectors. In: BLANCO, M. J.; SANTIGOSA, L. R. (Org.). **Advances in Concentrating Solar Thermal Research and Technology**, Amsterdam: Elsevier, 2017a.

MOYA, E. Zarza. Chapter 7: Parabolic-trough concentrating solar power (CSP) systems. In: LOVEGROVE, K.; STEIN, W. (Org.). **Concentrating solar power technology: Principles, developments and applications**, Cambridge, UK, Philadelphia, PA: Woodhead, 2012b.

PACHECO, J. E.; KOLB, W. j. **Comparison of an impedance heating system to mineral insulated heat trace for power tower applications**: Conference - SOLAR '97: national solar energy conference, Washington, DC (United States), 1997.

PARASCHIV, Spiru; PARASCHIV, Simona Lizica; PARASCHIV; ION, Ion V.; VATACHI, Nicușor. Design and sizing characteristics of a solar thermal power plant with cylindrical parabolic concentrators in Dobrogea region. *Revista Termotehnica*, 2010.

PATNODE, Angela M. **Simulation and Performance Evaluation of Parabolic Trough Solar Power Plants**, 2006.

PRICE, Hank; LÜPFERT, Eckhard; KEARNEY, David; ZARZA, Eduardo; COHEN, Gilbert; GEE, Randy; MAHONEY, Rod. Advances in Parabolic Trough Solar Power Technology. *Journal of Solar Energy Engineering*, v. 124, n. 2, p. 109, 2002.

QUASCHNING, Volker; KISTNER, Rainer; ORTMANN, Winfried. Influence of Direct Normal Irradiance Variation on the Optimal Parabolic Trough Field Size: A Problem Solved with Technical and Economical Simulations. *Journal of Solar Energy Engineering*, v. 124, n. 2, p. 160, 2002.

RAADE, Justin W.; PADOWITZ, David. Development of Molten Salt Heat Transfer Fluid With Low Melting Point and High Thermal Stability. *Journal of Solar Energy Engineering*, v. 133, n. 3, p. 31013, 2011.

RUEGAMER, T.; KAMP, H.; KUCKELKORN, T.; SCHIEL, W.; WEINREBE, G.; NAVA, P.; RIFFELMANN, K.; RICHERT, T. Molten Salt for Parabolic Trough Applications: System Simulation and Scale Effects. *Energy Procedia*, v. 49, p. 1523–1532, 2014.

SÁ, Alexandre Bittencourt de. **Procedimento para modelagem de uma planta termossolar utilizando a tecnologia de coletores cilindro parabólicos**, 2013.

SCHIEL, W.; SCHWEITZER, A.; KRACHT, O.; HUNT, B. **Collector Development for Parabolic trough Power Plants at Schlaich Bergermann und Partner**. Seville, Spain, 2006. (13th SolarPACES Conference).

SCHOTT SOLAR CSP. **SCHOTT PTR70 Receiver: The 4th Generation**, 2013. 12 p. Disponível em: <https://www.schott.com/d/csp/370a8801-3271-4b2a-a3e6-c0b5c78b01ae/1.0/schott_ptr70_4th_generation_brochure.pdf>.

SCHWEITZER, Axel; SCHIEL, Wolfgang; ABUL-ELLA, Zeyad; NAVA, Paul; RIFFELMANN, Klaus-Jürgen; WOHLFAHRT, Andreas; KUHLMANN, Gerd. **Ultimate Trough - The Next Generation Collector for Parabolic Trough Power Plants**. Granada, Spain, 2011. 9 p. (17th SolarPACES Conference).

STEINMANN, W.-D. Chapter 21: Thermal energy storage systems for concentrating solar power (CSP) technology. In: CABEZA, L. F. (Org.). **Advances in thermal energy storage systems: Methods and applications**, Boston MA: Elsevier, 2014.

THOMAS, A. Solar steam generating systems using parabolic trough concentrators. *Energy Conversion and Management*, v. 37, n. 2, p. 215–245, 1996.

VALLENTIN, Daniel; VIEBAHN, Peter. Economic opportunities resulting from a global deployment of concentrated solar power (CSP) technologies—The example of German technology providers. *Energy Policy*, v. 38, n. 8, p. 4467–4478, 2010.

VIEIRA, Leonardo dos Santos Reis; GUIMARÃES, Ana Paula Cardoso; BEZERRA, Lauro Barde; SERRA, Eduardo Torres. Projeto Básico de uma Central Heliotérmica de 1 MW em Petrolina-PE. *Revista Brasileira de Energia Solar*, 3/III, n. 1, p. 15–22, 2012. Acesso em: 4 jan. 2019.

WAGNER, Michael J.; GILMAN, P. **Technical Manual for the SAM Physical Trough Model**, 2011.

WAGNER, Michael. **Simulation and predictive performance modeling of utility-scale central receiver system power plants**. University of Wisconsin, 2008.

WAGNER, Patrick. **Thermodynamic simulation of solar thermal power stations with liquid salt as heat transfer fluid**, 2013.

WEATHER SPARK. Clima característico em Bom Jesus da Lapa, Brasil durante o ano. Disponível em: <<https://pt.weatherspark.com/y/30626/Clima-caracter%C3%ADstico-em-Bom-Jesus-da-Lapa-Brasil-durante-o-ano#Sections-Clouds>>. Acesso em: 18 jan. 2019.

WILCOX, Stephen. **National Solar Radiation Database 1991–2010 Update: User's Manual**, 2012. 479 p. Disponível em: <<https://www.nrel.gov/docs/fy12osti/54824.pdf>>. Acesso em: 31 dez. 2018.

WITTMANN, Michael; MÜLLER-ELVERS, Christian; SCHENK, Heiko; BRUCE, Barnaby. **Optimization of Molten Salt Parabolic Trough Power Plants using different Salt Candidates**. Marrakech, Morocco, 2012. (18th SolarPACES Conference).

ZAVOICO, ALEXIS B. **Solar Power Tower Design Basis Document: Revision 0**. Sandia National Laboratories (U.S.), 2001.

ZOGRAFOS, Antonios I.; MARTIN, William A.; SUNDERLAND, J.Edward. Equations of properties as a function of temperature for seven fluids. **Computer Methods in Applied Mechanics and Engineering**, v. 61, n. 2, p. 177–187, 1987.

APPENDIX A – MOLTEN SALT AND AIR THERMODYNAMIC PROPERTIES

Ferri, Cammi, Mazzei (2008) give the following set of equations for the molten salt properties for temperatures in Celsius:

- Density [kg / m^3]

$$\rho_{HTF} = 2090 - 0.636 \cdot (T - 273.15) \quad (A.1)$$

- Specific heat [$J / (kg \cdot ^\circ C)$]

$$c_{HTF} = 1443 + 0.172 \cdot T \quad (A.2)$$

- Dynamic viscosity [$N \cdot s / m^2$]

$$\mu_{HTF} = \frac{22.714 - 1.2 \times 10^{-1} \cdot T + 2.281 \times 10^{-4} \cdot T^2 - 1.474 \times 10^{-7} \cdot T^3}{1000} \quad (A.3)$$

- Thermal conductivity [$W / (m \cdot ^\circ C)$]

$$\kappa_{HTF} = 0.443 + 1.9 \times 10^{-4} \cdot T \quad (A.4)$$

The following equations used to describe the air properties, at atmospheric pressure and temperatures between 150K and 3000K, were adopted from Zografos, Martin, Sunderland (1987).

- Density [kg / m^3]

$$\rho_{air} = \frac{345.57}{T - 2.6884} \quad (A.5)$$

- Specific heat [$J / (kg \cdot ^\circ C)$]

$$c_{air} = 1.0613 \times 10^{-3} - 4.3282 \times 10^{-7} \cdot T - 1.0234 \times 10^{-9} \cdot T^2 - 6.4747 \times 10^{-13} \cdot T^3 + 1.3864 \times 10^{-16} \cdot T^4 \quad (A.6)$$

- Dynamic viscosity [$N \cdot s / m^2$]

$$\mu_{air} = 4.1130 \times 10^{-6} + 5.052364 \times 10^{-8} \cdot T - 1.4346 \times 10^{-11} \cdot T^2 + 2.5914 \times 10^{-15} \cdot T^3 \quad (A.7)$$

- Thermal conductivity [$W / (m \cdot ^\circ C)$]

$$\kappa_{air} = -7.488 \times 10^{-3} + 1.7082 \times 10^{-4} \cdot T + 2.2012 \times 10^{-10} \cdot T^2 - 2.3758 \times 10^{-7} \cdot T^2 + 9.46 \times 10^{-14} \cdot T^4 + 1.5797 \times 10^{-17} \cdot T^5 \quad (A.8)$$

APPENDIX B – HCE THERMAL RESISTANCES

B.1 CONDUCTION BETWEEN THE HTF AND THE ABSORBER TUBE

The thermal resistance for the forced convection inside the absorber tube (R_{HTF_abs}) can be calculated with equation B.1 where h'_{HTF_abs} is the heat transfer coefficient for the convection heat transfer between the HTF and the absorber tube and $D_{abs,i}$ is the absorber tube inner diameter.

$$R_{HTF_abs} = \frac{1}{h'_{HTF_abs} \cdot D_{abs,i} \cdot \pi} \quad (B.1)$$

The convection's heat transfer coefficient can be calculated through equation B.2 where Nu_{HTF} is the HTF's Nusselt number and κ_{HTF} is the HTF's thermal conductivity.

$$h'_{HTF_abs} = \frac{Nu_{HTF} \cdot \kappa_{HTF}}{D_{abs,i}} \quad (B.2)$$

There are different ways to obtain the HTF's Nusselt number depending on the flow regime developed inside the tube. The flow regime can be determined by estimating the Reynolds number (Re). In circular pipes, the flow is laminar for $Re < 2300$ or turbulent for $Re \geq 2300$. For the laminar regime, Forristall (2003) suggests assuming a uniform heat flow condition that leads to a constant Nusselt number with a value of 4.36.

On the other hand, Bergman, Lavine, Incropera (2011) indicates the Nusselt number can be calculated via the empiric equation of *Gnielinski* for varying conditions of turbulent flow, equation B.3. This mathematical relationship is valid for $2300 < Re_{abs,i} < 5 \times 10^6$ and $0.5 < Pr < 2000$.

$$Nu_{HTF} = \frac{\frac{f_f}{8} \cdot (Re_{abs,i} - 1000) \cdot Pr_{HTF}}{1 + \left(12.7 \cdot \sqrt{\frac{f_f}{8}} \cdot (Pr_{HTF}^{2/3} - 1) \right)} \cdot \left(\frac{Pr_{HTF}}{Pr_{abs,i}} \right)^{0.11} \quad (B.3)$$

where the f_f is the friction factor for a smooth tube inner surface, $Re_{abs,i}$ is the Reynolds number at the inner tube surface, Pr_{HTF} is the Prandtl number calculated at the HTF's temperature and $Pr_{abs,i}$ is the Prandtl number calculated at the absorbers inner surface temperature.

The friction factor is calculated via equation B.4, and the Reynolds number for the HTF' flow can be calculated by equation B.5 where \dot{m}_{HTF} is the HTF's mass flow rate inside the absorber tube and μ_{HTF} is the HTF's dynamic viscosity.

$$f_f = (1.82 \cdot \log_{10}(Re_{abs,i}) - 1.64)^{-2} \quad (\text{B.4})$$

$$Re_{abs,i} = \frac{4 \cdot \dot{m}_{HTF}}{\mu_{HTF} \cdot \pi \cdot D_{abs,i}} \quad (\text{B.5})$$

B.2 CONDUCTION THROUGH THE ABSORBER TUBE

The thermal resistance for the conduction through the absorber tube (R_{abs_abs}) can be obtained using equation B.6 where $D_{abs,o}$ is the absorber tube outer diameter and κ_{abs} is the absorber tube's thermal conductivity.

$$R_{abs_abs} = \frac{\ln\left(\frac{D_{abs,o}}{D_{abs,i}}\right)}{2\pi \cdot \kappa_{abs}} \quad (\text{B.6})$$

The absorber is made of stainless steel AISI 321 which thermal conductivity can be found via Equation B.7 where $T_{abs,o}$ and $T_{abs,i}$ are the temperature at the outer and inner surfaces of the absorber tube, respectively. This equation was obtained linearizing data from AK Steel (2012).

$$\kappa_{abs} = 1.5 \times 10^{-2} \cdot \left(\frac{T_{abs,i} + T_{abs,o}}{2} \right) + 14.5 \quad (\text{B.7})$$

B.3 RADIATION BETWEEN THE ABSORBER TUBE AND THE GLASS ENVELOPE

The thermal resistance for the radiation between the absorber tube and the glass envelope (R_{ans_env}) can be calculated with equation B.8 and equation B.9. In these equations, where h'_{abs_env} is the heat transfer coefficient for the radiation happening between the tube and the envelope, σ is the Stefan-Boltzmann constant, with the value of $5 \times 10^{-8} \text{ W}/(\text{m}^2 \cdot \text{K}^4)$, $T_{env,i}$ is the temperature at the inner surface of the glass envelope, $D_{env,i}$ is the glass envelope inner diameter, ε_{abs} is the absorber tube's emissivity and ε_{env} is the glass envelope's emissivity.

$$h'_{abs_env} = \frac{\sigma (T_{abs,o}^2 + T_{env,i}^2) \cdot (T_{abs,o} + T_{env,i})}{\left(\frac{1}{\zeta_{abs}} \right) + \frac{D_{abs,o}}{D_{env,i}} \cdot \left(\frac{1}{\zeta_{env}} - 1 \right)} \quad (\text{B.8})$$

$$R_{abs_env} = \frac{1}{h'_{abs_env} \cdot D_{abs,o} \cdot \pi} \quad (\text{B.9})$$

Both surfaces are considered gray and diffuse surfaces and both cylinders are considered concentric and long. The absorbers emissivity can be calculated by equation B.10 Archimede Solar Energy (2016).

$$\zeta_{abs} = 1.93 \times 10^{-4} \cdot T_{abs,i} - 7.73 \times 10^{-2} \quad (\text{B.10})$$

B.4 CONDUCTION THROUGH THE GLASS ENVELOPE

The thermal resistance for the conduction through the glass envelope's wall (R_{env_env}) can be calculated with equation B.11 where $D_{env,o}$ is the envelope's outer diameter and κ_{env} is the envelope's thermal conductivity.

$$R_{env_env} = \frac{\ln\left(\frac{D_{env,o}}{D_{env,i}}\right)}{2\pi \cdot \kappa_{env}} \quad (\text{B.11})$$

B.5 CONVECTION BETWEEN THE GLASS ENVELOPE AND THE ENVIRONMENT

The thermal resistance for the convective heat transfer between the glass envelope and the environment (R_{env_amb}) can be calculated with equation B.14 and equation B.13 where h'_{env_amb} is the heat transfer coefficient for convection between the glass envelope and the environment, Nu_{air} is the wind's Nusselt number, κ_{air} is the air's thermal conductivity and $D_{env,o}$ is the glass envelope's outer diameter.

$$h'_{env_amb} = \frac{Nu_{air} \cdot \kappa_{air}}{D_{env,o}} \quad (\text{B.12})$$

$$R_{env_amb} = \frac{1}{h'_{env_amb} \cdot \pi \cdot D_{env,o}} \quad (\text{B.13})$$

It is necessary to take a look in the ambient's wind flow characteristics to estimate the convective thermal resistance. Natural convection happens for wind speeds smaller than 0.1 m/s for which the Nusselt number can be calculated with equation B.14 and equation B.15 where $Ra_{env,o}$ is the Rayleigh number on the outer surface of the glass envelope, g is gravity's acceleration, β_{air} is the air's volumetric expansion coefficient (for an ideal gas), T_{amb} are the environment's dry bulb temperature and Pr_{air} the air flow's Prandtl number. For wind speeds larger than 0.1 m/s, forced convection happens and, therefore, the Nusselt number can be

calculated with equation B.16 which is recommended for Re_{air} and Pr_{air} larger than 0.2 Sá (2013). All air properties are calculated for temperature T_{air} , equation B.17.

$$Nu_{air,NConv} = \left[0.6 \cdot \frac{0.387 \cdot Ra_{env,o}^{1/6}}{\left(1 + (0.559 / Pr_{air})^{9/16}\right)^{8/27}} \right]^2 \quad (B.14)$$

$$Ra_{env,o} = \frac{g \cdot \beta_{air} \cdot \rho_{air} \cdot D_{env,o}^3 \cdot (T_{env,o} - T_{amb})}{\alpha_{air} \cdot \mu_{air}} \quad (B.15)$$

$$Nu_{air,FConv} = 0.3 + \frac{0.62 \cdot Re_{env,o}^{1/2} \cdot Pr_{air}^{1/3}}{\left[1 + (0.4 / Pr_{air})^{2/3}\right]^{1/4}} \cdot \left[1 + \left(\frac{Re_{env,o}}{282000}\right)^{5/8}\right]^{4/5} \quad (B.16)$$

$$T_{air} = \frac{T_{env,o} + T_{amb}}{2} \quad (B.17)$$

B.6 RADIATION BETWEEN THE GLASS ENVELOPE AND THE ENVIRONMENT

The thermal resistance for the radiation between the glass envelope and environment is calculated by equation B.18. According to Forristall (2003), it is common to assume the ambient as a black body at a corrected temperature T_{sky} , equation B.19.

$$R_{env_sky} = \frac{1}{\sigma \cdot \epsilon_{env} \cdot \pi \cdot D_{env,o} \cdot (T_{env,o}^2 + T_{sky}^2) \cdot (T_{env,o} + T_{sky})} \quad (B.18)$$

$$T_{sky} = T_{amb} - 8 \quad (B.19)$$

APPENDIX C – POWER BLOCK PHYSICAL MODEL

C.1 TURBINES

The high-pressure turbine receives, at its inlet, superheated steam at P_{PB1} and T_{PB1} . At both high-pressure and low-pressure turbines, a 5% mass flow extraction is made at each steam extraction point resulting in a total of 14.26% of the mass flow extracted to condensate heating and deaeration. This total extraction percentage is, as suggested by Wagner (2008), in the desirable range of 10% to 25% of total extraction.

To calculate the steam enthalpy at the extractions (h_{PB2} , h_{PB5} and h_{PB6}) as well as the steam enthalpy at each turbine outlet (h_{PB3} and h_{PB7}), the definition of isentropic efficiency is used as described by equation C.1 where g is the point number according to the numbering of figure 16 and the subscript s identifies an isentropic parameter. Furthermore, the gross power output, mechanical power, produced by each turbine can be calculated by equation C.2 and C.3, in W. The sum of these two give the total plant's gross power output (P_{gross}).

$$\eta_{turb} = \frac{h_{PB,g} - h_{PB,g-1}}{h_{PB,g,s} - h_{PB,g-1}} \quad (C.1)$$

$$\dot{W}_{HPturb} = 1000 \cdot [\dot{m}_{PB1} \cdot (h_{PB1} - h_{PB2}) + \dot{m}_{PB3} \cdot (h_{PB2} - h_{PB3})] \quad (C.2)$$

$$\dot{W}_{LPturb} = 1000 \cdot [\dot{m}_{PB3} \cdot (h_{PB4} - h_{PB5}) + \dot{m}_{PB5} \cdot (h_{PB5} - h_{PB6}) + \dot{m}_{PB6} \cdot (h_{PB6} - h_{PB7})] \quad (C.3)$$

C.2 GROSS TO NET CONVERSION

In this work, the conversion of gross to net power output accounts more than just the mechanical to electrical efficiency. Biencinto et al. (2014) considers a gross to net power output conversion efficiency ($\eta_{gross_to_net}$) of 0.88 - accounting on it generator and transformer electrical losses, additional parasitic losses, solar field inoperability during certain periods of the year due to excessive wind speeds and other factors that can make the plant not available for power production - while deducting the solar field HTF pump's parasitic losses directly from the gross power output. Therefore, as in this work no parasitic loss was calculated, a gross to net power output conversion efficiency of 0.85 was considered. Equation C.4 calculates the plant's net power output.

$$P_{net} = \eta_{gross_to_net} \cdot P_{gross} = \eta_{gross_to_net} \cdot (\dot{W}_{HPturb} + \dot{W}_{LPturb}) \quad (C.4)$$

C.3 CONDENSER

The condenser, as well as the other heat exchanger applied, are assumed to be single pass counterflow shell and tube heat exchangers, an analog case of the double tube heat exchanger, in which the water/vapor from the Rankine cycle passes through the tubes. This model will assume wet cooling. It is assumed that the condensate leaves the condenser as a saturated liquid. The thermal energy discharged from the cycle in the condenser can be calculated, in W, with equation C.5. The overall heat transfer coefficient for the condenser can be estimated through the ε -NTU (Effectiveness/Number of Transfer Units) method as described by Bergman, Lavine, Incropera (2011), equation C.6 to equation C.10.

$$\dot{q}_{cond} = 1000 \cdot \dot{m}_{PB7} \cdot (h_{PB7} - h_{PB8}) = 1000 \cdot \dot{m}_{PB18} \cdot (h_{PB19} - h_{PB18}) \quad (C.5)$$

$$C_{cond,min} = 1000 \cdot \dot{m}_{PB18} \cdot c_{cond,cold} = 1000 \cdot \dot{m}_{PB18} \cdot \left(\frac{h_{PB18} - h_{PB19}}{T_{PB18} - T_{PB19}} \right) \quad (C.6)$$

$$\dot{q}_{cond,max} = C_{cond,min} \cdot (T_{PB7} - T_{PB18}) \quad (C.7)$$

$$\varepsilon_{cond} = \frac{\dot{q}_{cond}}{\dot{q}_{cond,max}} \quad (C.8)$$

$$NTU_{cond} = -\ln(1 - \varepsilon_{cond}) \quad (C.9)$$

$$UA_{cond} = NTU_{cond} \cdot C_{cond,min} \quad (C.10)$$

C.4 PUMPS

While the pumps that precede the mixing vessels and deaerator act to higher the pressure of the feedwater to the same pressure of those vessels, which are actually the pressure of the extractions they receive, the pump that precede the heat exchanger's train is used to higher the pressure of the feedwater to the high-pressure turbine inlet. The enthalpy post pump can be calculated using the pump's isentropic efficiency definition, equation C.11. Moreover, an isentropic efficiency of 0.68 is assumed for all pumps in the Rankine cycle.

$$\eta_{pump} = \frac{h_{PB,g-1} - h_{PB,g,s}}{h_{PB,g-1} - h_{PB,g}} \quad (C.11)$$

C.5 MIXING VESSELS AND DEAERATOR

In the mixing vessels and the deaerator, the outlet flow is always saturated liquid, the outlet mass flow rate is equal to the sum of the feed-water, and vapor extraction mass flows,

and the outlet temperature is the average of the temperatures of both flows weighted by the mass flow rates.

C.6 MOLTEN SALT HEAT EXCHANGERS

The heat exchangers that transfer heat from the molten salts to the Rankine cycle water are shell and tube exchangers in which the molten salt is put in counterflow to the water through the shell side (ZAVOICO, 2001). The heat exchangers modeled can be divided in heat exchanger train, economizer, evaporator, and superheater, and reheater. The heat exchanged through these exchangers are described by equation C.12 to equation C.15, in W.

$$\dot{q}_{eco} = \dot{m}_{PB1} \cdot (h_{PB16} - h_{PB15}) \cdot 1000 \quad (C.12)$$

$$\dot{q}_{eva} = \dot{m}_{PB1} \cdot (h_{PB17} - h_{PB16}) \cdot 1000 \quad (C.13)$$

$$\dot{q}_{sup} = \dot{m}_{PB1} \cdot (h_{PB1} - h_{PB17}) \cdot 1000 \quad (C.14)$$

$$\dot{q}_{reh} = \dot{m}_{PB3} \cdot (h_{PB4} - h_{PB3}) \cdot 1000 \quad (C.15)$$

The molten salt heat exchanger's overall heat transfer coefficients can be calculated using the ε -NTU method. The heat transfer coefficient from the economizer can be calculated using equation C.16 to equation C.24. The heat transfer coefficient for the superheater and the reheater can be calculated using the same set of equations described for the economizer but exchanging the thermodynamic cycle points necessary. The evaporator's heat transfer coefficient can be calculated with the same set of equations used for the condenser as in the evaporator the water also undergoes a phase change.

$$C_{eco,hot} = \dot{m}_{PB20} \cdot C_{HTF,eco} \left(\frac{T_{PB24} + T_{PB23}}{2} \right) \quad (C.16)$$

$$C_{eco,cold} = 1000 \cdot \dot{m}_{PB1} \cdot C_{eco,cold} = 1000 \cdot \dot{m}_{PB1} \cdot \left(\frac{h_{PB16} - h_{PB15}}{T_{PB16} - T_{PB15}} \right) \quad (C.17)$$

$$C_{eco,min} = \min(C_{eco,hot}, C_{eco,cold}) \quad (C.18)$$

$$C_{eco,max} = \max(C_{eco,hot}, C_{eco,cold}) \quad (C.19)$$

$$\dot{q}_{eco,max} = C_{eco,min} \cdot (T_{PB22} - T_{PB15}) \quad (C.20)$$

$$\varepsilon_{eco} = \frac{\dot{q}_{eco}}{\dot{q}_{eco,max}} \quad (C.21)$$

$$C_{r,eco} = \frac{C_{eco,min}}{C_{eco,max}} \quad (C.22)$$

$$NTU_{eco} = \left(\frac{1}{C_{r,eco} - 1} \right) \cdot \ln \left(\frac{\varepsilon_{eco} - 1}{\varepsilon_{eco} \cdot C_r - 1} \right) \quad (C.23)$$

$$UA_{eco} = NTU_{eco} \cdot C_{eco,min} \quad (C.24)$$

C.7 CYCLE EFFICIENCY

The cycle efficiency can be calculated via Equation D.8.

$$\eta_{PB} = \frac{P_{gross}}{\dot{q}_{eco} + \dot{q}_{eva} + \dot{q}_{sup} + \dot{q}_{reh}} \quad (C.25)$$

C.8 DESIGN PARAMETERS

Some cycle design parameters were imposed as described in table C.1. These parameters were chosen so that the simulation could be performed and the rest of the thermodynamic cycle nominal parameters could be found.

Table C.1 - Rankine cycle design parameters

Parameter	Value	Unit
P_{net}	30	MW
P_{PB1}	100	bar
P_{PB2}	50	bar
P_{PB3}	15	bar
P_{PB4}	15	bar
P_{PB5}	8.5	bar
P_{PB6}	2.5	bar
P_{PB7}	0.1	Bar
T_{PB1}	540	°C
T_{PB18}	25	°C
T_{PB19}	35	°C
T_{PB20}	550	°C
T_{PB24}	550	°C
T_{PB25}	360	°C